Advances in Mechanical Engineering

Two-Phase Flow and Heat Transfer Enhancement

Guest Editors: Somchai Wongwises, Afshin J. Ghajar, Kwok-wing Chau, Octavio García Valladares, Balaram Kundu, Ahmet Selim Dalkılıç, and Godson Asirvatham Lazarus

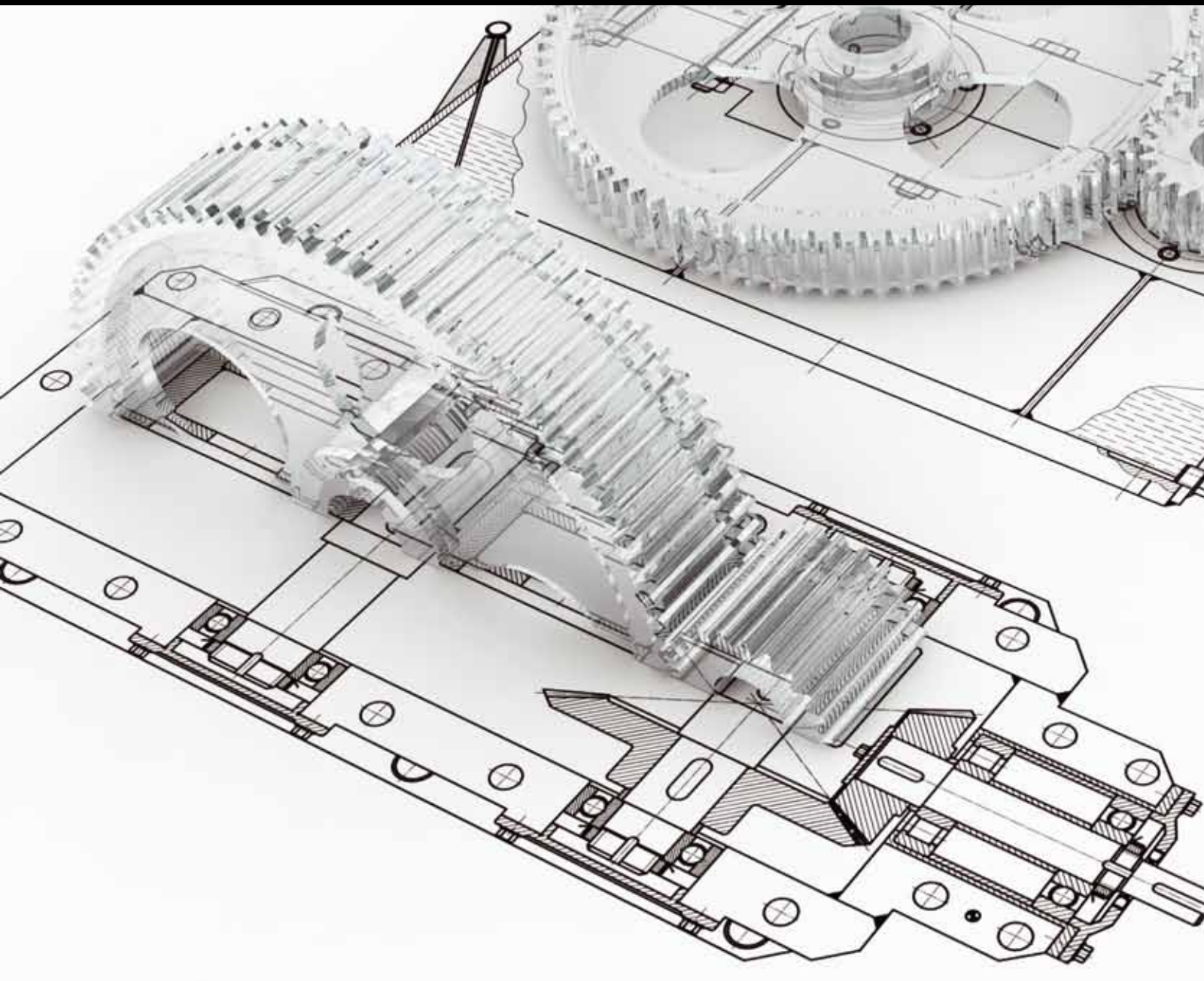

Two-Phase Flow and Heat Transfer Enhancement

Advances in Mechanical Engineering

Two-Phase Flow and Heat Transfer Enhancement

Guest Editors: Somchai Wongwises, Afshin J. Ghajar, Kwok-wing Chau, Octavio García Valladares, Balaram Kundu, Ahmet Selim Dalkılıç, and Godson Asirvatham Lazarus

Editorial Board

Contents

Hindawi Publishing Corporation
Advances in Mechanical Engineering
Volume 2013, Article ID 256839, 2 pages
http://dx.doi.org/10.1155/2013/256839

Editorial
Two-Phase Flow and Heat Transfer Enhancement

Somchai Wongwises,[1] Afshin J. Ghajar,[2] Kwok-wing Chau,[3] Octavio García Valladares,[4] Balaram Kundu,[5] Ahmet Selim Dalkılıç,[6] and Godson Asirvatham Lazarus[7]

[1] *Fluid Mechanics, Thermal Engineering and Multiphase Flow Research Lab. (FUTURE), Department of Mechanical Engineering, Faculty of Engineering, King Mongkut's University of Technology Thonburi, Bangmod, Bangkok 10140, Thailand*
[2] *School of Mechanical and Aerospace Engineering, Oklahoma State University, Stillwater, OK 74078, USA*
[3] *Department of Civil & Environmental Engineering, The Hong Kong Polytechnic University Hunghom, Kowloon, Hong Kong*
[4] *Department of Energy Systems, Centro de Investigación en Energía, CIE-UNAM, Privada Xochicalco S/N, 62580 Temixco, MOR, Mexico*
[5] *Department of Mechanical Engineering, Jadavpur University, Kolkata 700032, India*
[6] *Heat and Thermodynamics Division, Department of Mechanical Engineering, Yildiz Technical University, Yildiz, 34349 Istanbul, Turkey*
[7] *Department of Mechanical Engineering, Karunya University, Coimbatore, Tamil Nadu 641 114, India*

Correspondence should be addressed to Somchai Wongwises; somchai.won@kmutt.ac.th

Received 2 December 2013; Accepted 2 December 2013

Gas-liquid two-phase flow and heat transfer processes are commonly encountered in a wide variety of applications, for example, refrigeration and air-conditioning systems, power engineering, and other thermal processing plants. The advantage of high thermal performance in comparison to the single-phase applications leads to various engineering applications including the cooling systems of various types of equipment such as high performance microelectronics, supercomputers, high-powered lasers, medical devices, high heat-flux compact heat exchangers in spacecraft and satellites, and so forth. The aim of this special issue was to collect the original research and review papers on the recent developments in the field of two-phase flow and heat transfer enhancement. Potential topics included advanced heat pipe technologies, boiling and condensation heat transfer, CHF and post-CHF heat transfer, cooling of electronic system, Heat and mass transfer in phase change processes, instabilities of two-phase flow, measurements and modeling of two-phase flow in microchannel, microgravity in two-phase flow, nanofluids science and technology, nuclear reactor applications, passive and active heat transfer enhancement techniques, Refrigeration and air-conditioning technology, two-phase flow with heat and mass transfer, two-phase refrigerant flow, and special topics on the latest advances in two-phase flow and heat transfer. In this special issue, we have invited a few papers that address such issues.

First paper of special issue investigates the effect of convergence angle of microchannel on two-phase flow and heat transfer during steam condensation experimentally. The experimental results show that the condensation heat flux increases with an increase in the convergence angle and/or the steam mass flux at a given coolant flow rate but decreases with an increase in the coolant flow rate at a given steam mass flux. Second paper focuses on simulating mist impingement cooling under typical gas turbine operating conditions of high temperature and pressure in a double chamber model. The results of this paper can provide guidance for corresponding experiments and serve as the qualification reference for future more complicated studies with convex surface cooling. In third paper, economic analysis of rebuilding an aged pulverized coal-fired boiler with a new pulverized coal-fired boiler including flue gas desulfurization unit and a circulating fluidized bed boiler is investigated in existing old thermal power plants. The fourth paper presents the results of a CFD analysis and experimental tests of two identical miniature flat plate heat pipes using sintered and screen

mesh wicks and a comparative analysis and measurement of two solid copper base plates 1 mm and 3 mm thick. In fifth paper, a modeled room was numerically heated from a wall and cooled from the opposite wall in order to create a real-room simulation. The cooled wall simulated heat loss of the room, and the heated wall simulated the heat source of enclosure. The effects of heated and cooled wall temperatures on convective heat transfer coefficient and Nusselt number in the enclosure were investigated numerically for two- and three-dimensional (3D) modeling states.

In summary, this special issue reflects a variety of contemporary research in heat transfer and is expected to promote further research activities and development opportunities.

Acknowledgment

We thank the authors who prepared the paper within the stringent length and time requirements. We thank the reviewers who provided meaningful suggestions on short notice.

Somchai Wongwises
Afshin J. Ghajar
Kwok-wing Chau
Octavio García Valladares
Balaram Kundu
Ahmet Selim Dalkılıç
Godson Asirvatham Lazarus

Hindawi Publishing Corporation
Advances in Mechanical Engineering
Volume 2013, Article ID 372898, 10 pages
http://dx.doi.org/10.1155/2013/372898

Research Article

Two-Phase Flow and Heat Transfer during Steam Condensation in a Converging Microchannel with Different Convergence Angles

Ben-Ran Fu,[1] T. H. Chang,[2] and Chin Pan[2,3,4]

[1] *Green Energy and Environment Research Laboratories, Industrial Technology Research Institute, Hsinchu 31040, Taiwan*
[2] *Department of Engineering and System Science, National Tsing Hua University, Hsinchu 30013, Taiwan*
[3] *Institute of Nuclear Engineering and Science, National Tsing Hua University, Hsinchu 30013, Taiwan*
[4] *Low Carbon Energy Research Center, National Tsing Hua University, Hsinchu 30013, Taiwan*

Correspondence should be addressed to Chin Pan; cpan@ess.nthu.edu.tw

Received 15 June 2013; Revised 30 September 2013; Accepted 30 September 2013

Academic Editor: Ahmet Selim Dalkılıç

The present study experimentally investigates the effect of convergence angle of microchannel on two-phase flow and heat transfer during steam condensation. Three condensation regimes, from the inlet to the outlet, are identified: mist/annular flow, injection flow, and slug-bubbly flow. Flow pattern maps are constructed using superficial vapor and liquid velocities as the coordinates, wherein relatively distinct boundaries between the flow patterns can be identified. The experimental results show that the condensation heat flux increases with an increase in the convergence angle and/or the steam mass flux at a given coolant flow rate but decreases with an increase in the coolant flow rate at a given steam mass flux. The results further demonstrate that the local condensation heat transfer coefficient in the mist/annular flow region is much higher than that in other condensation regimes. Moreover, the local condensation heat transfer coefficient in the mist/annular flow and injection flow region decreases with an increase in the convergence angle.

1. Introduction

Condensation in microchannels is of significant fundamental interest and has diversified applications, such as in microchannel heat exchangers and micro-fuel cells. In recent years, many studies on the characteristics of two-phase flow and heat transfer during condensation in microchannels were reported. For example, Wu and Cheng [1] visualized the condensation flow patterns of steam flowing through 10 parallel microchannels with a hydraulic diameter of 82.8 μm and a trapezoidal cross-sectional area. They categorized the flow patterns observed as follows: droplet flow (mist flow), annular flow, injection flow, and slug-bubbly flow. The injection flow pattern appears periodically because of its upstream flow patterns alternate between the droplet two-phase flow and the vapor flow. Wu et al. [2] further carried out experimental studies on injection flow during steam condensation in microchannels with hydraulic diameters ranging from 53 μm to 128.5 μm. They proposed that the location of the injection flow corresponds to the Reynolds number (Re), condensation number (Co), and diameter-to-length ratio (D_h/L) and obtained a dimensionless correlation for the location of injection flow in silicon microchannels.

Quan et al. [3] investigated the effects of the mass flux and cooling flow rate on the occurrence frequency of the injection flow in a single microchannel with hydraulic diameters of 120 and 128 μm. Their study revealed that the shape of the microchannels has a critical influence on the instability of the condensation flow mechanisms. Furthermore, Wu et al. [4] conducted an experimental study on heat transfer and flow friction during steam condensation in trapezoidal silicon microchannels with hydraulic diameters of 77.5, 93.0, and 128.5 μm. Their experimental results demonstrated that the condensation Nusselt number increases with an increase in the Re, Co, and D_h/L, and the condensation two-phase

frictional multiplier decreases with an increase in the Re and D_h/L or a decrease in the Co.

Chen et al. [5] performed a visualization experiment to investigate the steam condensation in triangular microchannels with hydraulic diameters of 100 and 250 μm. The experimental results indicated that the droplet, annular, injection, and slug-bubbly flows are the dominant flow patterns during steam condensation in microchannels. In addition, they proposed the correlations for injection location, injection frequency, and condensation Nusselt number. Wu et al. [6] presented a visualization study on steam condensation in wide rectangular microchannels. Three typical flow patterns were identified in their study, namely, droplet-annular compound flow, injection flow, and vapor slug-bubbly flow. They demonstrated that the injection location moves to the channel outlet with an increase in the Re, and the injection frequency increases with increasing the Re and condensate Weber number. In addition, the results showed that the injection frequency is lower than that in the triangular microchannel with the same hydraulic diameter, indicating that the cross-sectional shape of the microchannel plays an important role in the instability of condensation flow.

Agarwal et al. [7] reported the condensation heat transfer coefficients of R134a in six noncircular horizontal microchannels with different shapes (barrel-shaped, N-shaped, rectangular, square, and triangular tubes, and a channel with a W-shaped corrugated insert). For square, rectangular, and barrel-shaped channels, an annular-flow-based heat transfer model was developed. On the other hand, for triangular, N-shaped, and W-insert channels (i.e., those with sharp corner), a mist-flow-based heat transfer model was proposed. Ma et al. [8] investigated the two-phase flow patterns and transition characteristics during steam condensation in trapezoidal microchannels. Annular flow, droplet flow, injection flow, and bubbly flow were observed in their study. Two-phase flow pattern maps were constructed using coordinates of steam mass flux and steam quality. They also reported that the flow pattern transition from annular flow to bubbly flow occurs earlier in the smaller microchannel. In addition, criteria for transitions between flow patterns were also proposed in the form of nondimensional groups (steam quality, condensation number, Reynolds number, Weber number, Bond number, and width-to-diameter ratio).

Fang et al. [9] investigated the effect of wall hydrophobicity on the steam condensation in the rectangular microchannel. They found that the channel surface wettability has a significant impact on the condensation flow pattern, pressure drop, and heat transfer characteristics. At a given inlet vapor flux and temperature, the hydrophobic microchannel presents higher heat transfer rate and pressure drop than those in the hydrophilic one. Odaymet and Louahlia-Gualous [10] reported the local heat transfer coefficient and flow visualization during condensation in a square microchannel. They identified the following flow regimes: mist flow, churn flow, annular flow, slug flow, liquid ring flow, and annular/bubbly flow. Their results indicated that the local condensation heat transfer coefficient increases with an increase in the steam mass flux. Recently, Odaymet et al. [11] investigated the local heat transfer and flow patterns during steam condensation in a single silicon-based microchannel. They further modified condensation flow patterns as follows (from upstream to downstream): mist flow, churn flow, elongated bubbly flow followed by a bubbly sequence, and slug flow. In addition, they also found that local thermal performance of condensation flow for mist flow and upstream elongated bubbly flow is better than slug and bubbly flows.

Kim et al. [12] carried out an experimental study on condensation of FC-72 in parallel microchannels. Smooth-annular, wavy-annular, transition, slug, and bubbly flows were identified in their experimental observation. Furthermore, they discussed the condensation two-phase flow pressure drop using both two-phase homogenous and separated flow models and found that the homogenous model unexpectedly provides better predictions than the separated flow model. Furthermore, Kim and Mudawar [13] demonstrated that the local condensation heat transfer coefficient is the highest near the channel inlet and decreases along the microchannel due to an increase in the film thickness. In addition, a correlation of condensation heat transfer coefficient for annular condensation in microchannels was also proposed.

Based on the above literature reviews on microchannel condensation, it is clearly found that significant effects of microchannel cross-sectional shape on the condensation flow patterns and heat transfer are demonstrated. In our previous study [14], convective steam condensation in uniform, converging, and diverging microchannels with a mean hydraulic diameter of 117 μm was experimentally investigated. The steam flow in the microchannel was cooled by a still water bath. Flow patterns, two-phase flow pressure drop, outlet temperature, bubbly emission frequency, and bubbly velocity in the three different cross-section designs of microchannels were reported. The experimental results demonstrated that, for a given steam mass flow rate, the two-phase flow pressure drop in the diverging microchannel is considerably higher than that in the uniform and converging microchannels. The converging microchannel presents the lowest two-phase flow pressure drop, suggesting its merit for removing the two-phase fluids during steam condensation.

Furthermore, Kuo and Pan [15] investigated steam condensation in uniform and converging microchannels with a mean hydraulic diameter of 135 μm. The steam flow in the microchannels was cooled by water cross-flowing along its bottom surface, which is different from other methods reported in the literature. The flow patterns, two-phase flow pressure drop, and local condensation heat transfer coefficient were examined. The results demonstrated that although the uniform microchannel presents a higher heat transfer coefficient than those in the converging microchannel under mist/annular flow regimes, the total heat transfer rate is higher for the microchannel with the converging cross-section than that with the uniform cross-section. Moreover, empirical correlations of local condensation heat transfer for the mist and annular flow regions and a two-phase frictional multiplier in the form of the Lockhart-Martinelli correlation were developed.

This work investigates the effect of convergence angle (half of the included angle) of microchannel experimentally

on two-phase flow and heat transfer during steam condensation. Flow pattern maps are constructed using coordinates of superficial vapor and liquid velocities. In addition, the effects of convergence angle on local heat transfer coefficient as well as condensation heat transfer rate are explored.

2. Experimental Details

2.1. Experimental Setup. Figure 1 shows the experimental setup, which is similar to that employed in our previous study [15], that consists of a water tank, a high-performance liquid chromatography (HPLC) pump (P680: Dionex), a heating module, a test section, a cooling water circulation system, a condensate collecting container, an electronic balance (XS625 M: Precisa Gravimetrics), a flow visualization system, and related control and measurement systems. Before conducting experiments, the deionized water in the water tank was boiled to evacuate dissolved gas. Then, water was driven by the HPLC pump through the helical tube immersed in the silicone oil bath and heated and stirred by a heating module to vaporize the water to steam. The steam subsequently flowed into the test section. Three K-type thermocouples were placed in the bath to measure the oil temperature. A cooling water circulation system combined with a metering pump (FEM03KT: KNF) drove water with a constant inlet temperature of 22°C at a specific flow rate in the cross-flow direction along the backside surface of the test section. The condensate was collected by a container at atmosphere pressure and condensate was weighed using an electronic balance to verify the steam mass flow rates (m_s). The steam mass flow rates in the present study ranged from 2.36×10^{-6} kg/s to 5.28×10^{-6} kg/s.

The test section with a converging microchannel was a silicon strip with dimensions of 10 mm × 48 mm. Three convergence angles ($\beta = 0.5^\circ, 1.0^\circ$, and 1.5°) of the microchannel with the same mean hydraulic diameter (D_h) of 135 μm were employed to study the effect of convergence angle. Here, the mean hydraulic diameter of the converging microchannel was calculated based on the following definition [16]:

$$D_h = \frac{1}{L}\int_0^L \frac{4 \times H \times W(x)}{2 \times [H + W(x)]}\, dx = 2H\left[1 - \frac{H}{W_{\text{out}} - W_{\text{in}}} \ln\left(\frac{H + W_{\text{out}}}{H + W_{\text{in}}}\right)\right]. \quad (1)$$

Figures 2 and 3 depict schematics of the test section and cooling chamber, respectively. The detailed dimensions of the microchannels with different convergence angles are summarized in Table 1. Two T-type thermocouples and a differential pressure transducer (692: Huba) were employed to measure the inlet and outlet temperatures and the pressure drop between the inlet and outlet chambers. Three T-type thermocouples were embedded in the backside surface of the test section (facing the coolant) to measure the local wall temperature (T_w), which is then used to evaluate the local heat transfer coefficient. These three thermocouples were located at z = 9.5, 17.5, and 25.5 mm, respectively, in reference to the channel inlet. The data of the thermocouples and the differential pressure transducer were recorded by a data acquisition system (MX100: Yokogawa) with a sampling rate of 2 Hz.

Table 1: Detailed dimensions of the microchannels with different convergence angles.

Test section	Ref. [15]	No. 1	No. 2	No. 3
β (°)	0	0.5	1.0	1.5
W_{in} (μm)	675	1022	1445	1933
W_{out} (μm)	675	410	220	100
L (mm)	35	35	35	35
H (μm)	75	75	75	75
D_h (μm)	135	135	135	135

The flow visualization system included a high-speed digital camera (XS-4: IDT) mounted with a microlens (zoom 125C: OPTEM) and a computer. In addition, an x-y-z mechanism was installed to hold the CCD and microlens with an accurate position on the test plane (x-y plane) and focus in the z-direction. The typical frame rate employed in the study was 4000 frames/s. A 250 W fiber optic illuminator (FOI-250: TechniQuip) was used as the light source.

2.2. Fabrication of the Test Section. To prepare the microchannel with a uniform depth, the test section was made of P-type (100) orientation silicon on insulator (SOI) wafer, which consisted of three layers (from bottom to top): (1) handle layer (P-type (100) bare wafer, thickness: 525 ± 25 μm); (2) box layer (SiO_2, thickness: 0.5 μm); and (3) device layer (P-type (100) silicon wafer, thickness: 75 ± 1 μm). The converging microchannels with inlet and outlet chambers were etched on the surface of the device layer. The fabrication processes of the test section employed deep reactive ion etching (DRIE) with photolithography, laser-cutting technology, and anodic bonding processes. The etching stop mechanism on the box layer for the DRIE process ensured a uniform depth for the microchannels and chambers. Subsequently, an excimer laser micromachining technology was applied to make through holes, which were used as the inlet and outlet chambers for the working fluid to flow through the microchannel. Finally, to enable flow visualization the test section was covered with the Pyrex no. 7740 glass through anodic bonding.

2.3. Uncertainty Analysis. The measurement uncertainty for the liquid volumetric flow rate through the HPLC pump in the microchannels after calibration was estimated to be ±0.2%. The accuracy of the metering pump was ±2%. The measurement uncertainty of the pressure transducer was 0.5% over the full scale, resulting in an actual uncertainty of ±1.25 kPa. The uncertainties in the temperature measurements were ±0.2°C and ±0.5°C for T-type and K-type thermocouples, respectively. The ambient temperature was controlled at about 25°C by an air conditioner during experiments. The uncertainties for the temperature of the cooling water, ambient condition, and steam were estimated to be ±0.5°C. The uncertainty analysis methodology developed by Moffat [17] was used to estimate the uncertainty for the total condensation heat transfer rate and the local condensation

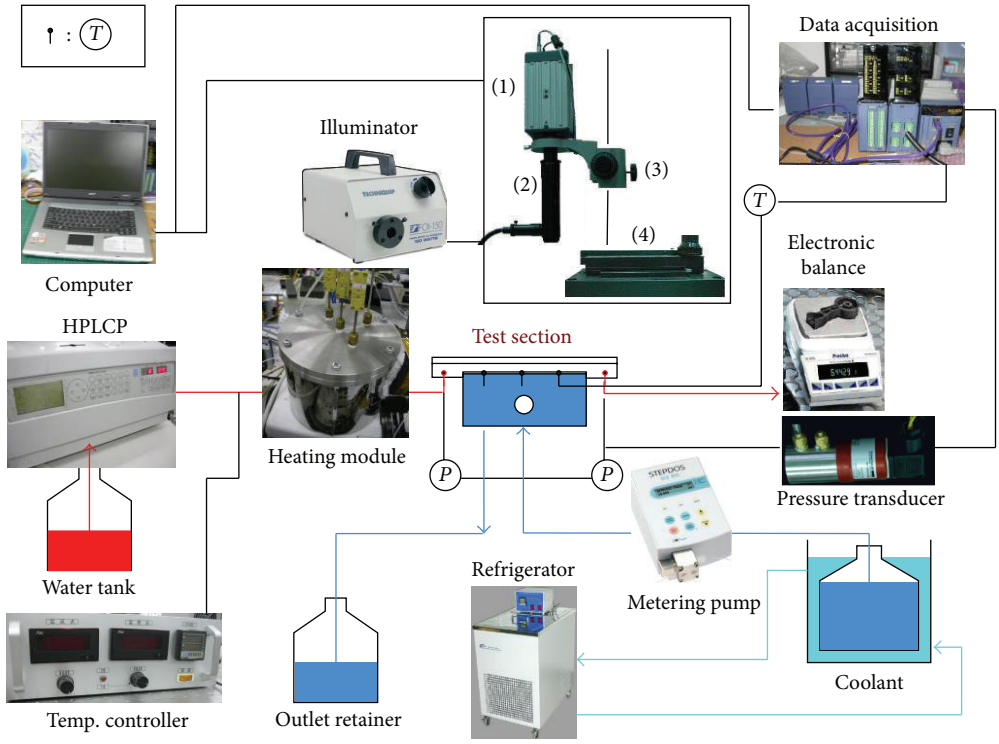

Figure 1: Experimental setup: (1) CCD, (2) microscope, and (3) and (4) x-y-z mechanism.

heat transfer coefficient, which were 1.9% and 6.6%, respectively. In addition, the uncertainty of the void fraction of 0.52 is about 9.6%, estimated from our previous study [18], which is due to the image analysis tool. As shown in Fu et al. [18], the uncertainty of the void fraction decreases with an increase in the void fraction. Consequently, the uncertainty for the void fraction of 0.8, which is corresponding to transition location between mist/annular flow and injection flow, will be smaller than 9.6%. And the highest uncertainty of the condensation heat transfer rate for a particular flow region is 9.8%, which is higher than that of total condensation heat transfer rate.

3. Data Reduction

In the present study, the heat released by the steam is mainly carried away by the forced convection to the cooling water flowing underneath the test section, defined as q_c, and a small fraction may be lost by natural convection via the top glass surface of the test section to the ambient air. In the present study, the estimated heat transfer by natural convection is less than 0.1% of the measured heat dissipation. Thus, the total heat (q_t) released by the steam can be reasonably considered to be absorbed totally by the coolant (q_c); that is, $q_t = q_c$. Thermal radiation to the ambient is considered to be negligible. Here, q_c is estimated by the following equations:

$$q_c = m_c c_{p,c} \left(T_{c,\text{out}} - T_{c,\text{in}}\right). \tag{2}$$

Following a methodology developed by Kuo and Pan [15], the total condensation heat transfer rate along the microchannel is divided into three parts, that is, q_1, q_2, and q_3, corresponding to three distinct two-phase flow regimes: (1) the mist/annular flow, (2) injection flow, and (3) slug/bubbly flow regions, respectively, as depicted in Figure 4. These three regions can be distinguished clearly by flow visualization. Consider

$$q_t = q_1 + q_2 + q_3. \tag{3}$$

The distributions of the condensation heat transfer rate in regions (1) and (3) are assumed to be uniform. For region (1), mist/annular flow prevails and the void fraction is close to unity. Therefore, it is reasonable to assume a uniform condensation heat transfer rate there. On the other hand, for region (3) bubbly flow appears, and thus the condensation heat transfer rate is low and is also uniformly distributed. The condensation heat transfer rates in regions (1) and (3) can be evaluated by the following equations based on the energy balance with a vapor quality (x) determined from the void fraction (α) data:

$$\begin{aligned} q_1 &= \left(x_{\text{in}} - x_1\right) m_s i_{\text{LV}} \\ q_3 &= \left(x_2 - x_{\text{out}}\right) m_s i_{\text{LV}}, \end{aligned} \tag{4}$$

where vapor quality at any axial location, z, can be estimated from the following equations:

$$\alpha_z = \frac{0.03\alpha_{h,z}^{0.5}}{1 - 0.97\alpha_{h,z}^{0.5}}, \tag{5}$$

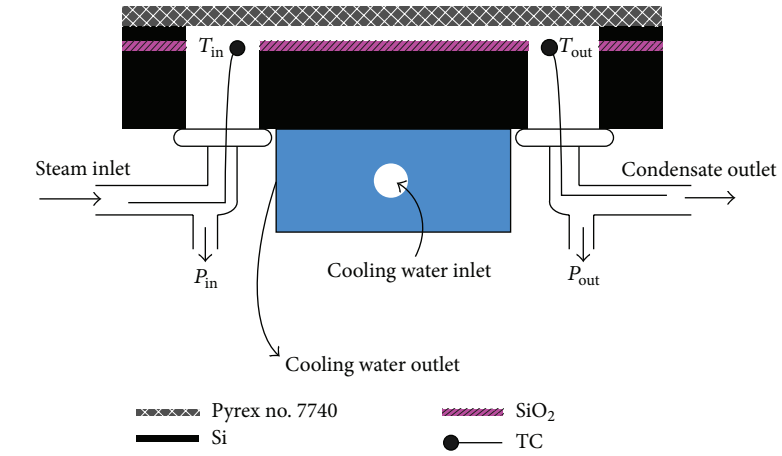

(a)

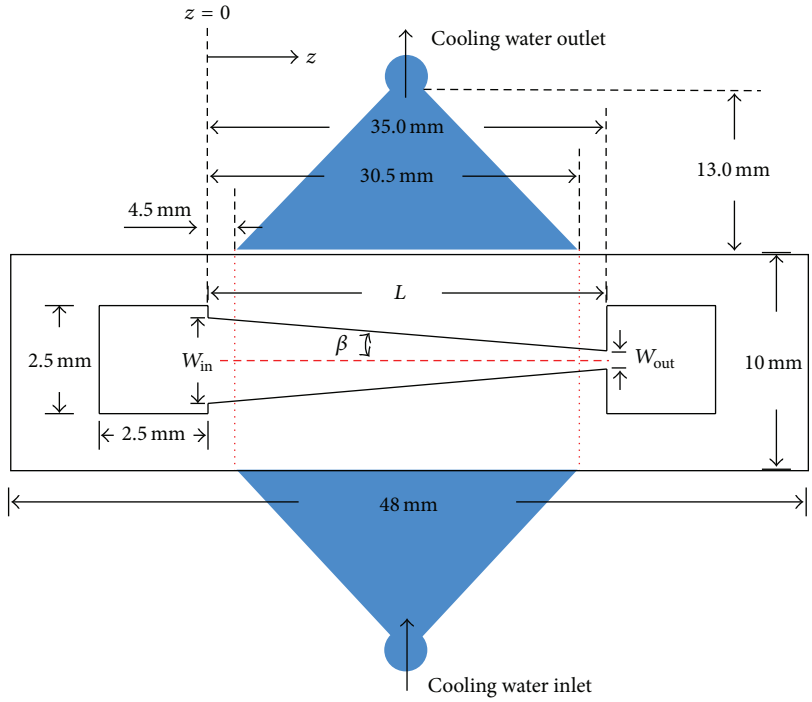

(b)

Figure 2: Schematic of the test section: (a) side view and (b) top view.

proposed by Kawahara et al. [19]. Consider

$$\alpha_{h,z} = \frac{j_{V,z}}{j_{V,z} + j_{L,z}} = \frac{1}{1 + (1/x_z - 1)\,\rho_V/\rho_L}$$
$$x_{in} = x_{out} + \frac{q_t}{m_s i_{LV}}. \quad (6)$$

For the present study, the void fraction for a particular region is determined by the mean value of the projected area of vapor bubbles on the bottom wall of 100 frames, randomly selected from the flow visualization of different conditions, divided by the bottom surface area of the region [18]. The present results demonstrate that the void fraction decreases sharply during the injection flow and keeps nearly constant toward the channel outlet, as reported in our previous study [15]. The persistence of such a nearly constant void fraction near the channel outlet reflects the poor condensation heat transfer therein, which will be demonstrated later. Given local void fraction determined, the corresponding vapor quality and local condensation heat flux in each region may then be determined.

After the condensation heat transfer rates in different regions are obtained, the local condensation heat transfer coefficient can be estimated on the basis of the temperature

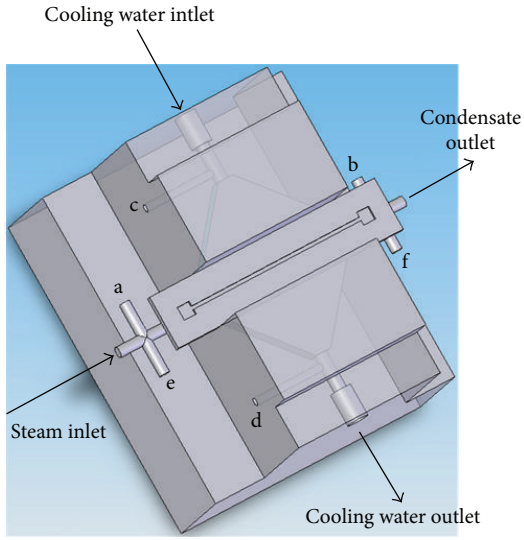

Figure 3: Schematic of the test section combined with a cooling chamber. Locations "a" to "d" are points for temperature measurement and "e" and "f" are pressure tap locations in the microchannel.

difference between the saturation temperature ($T_{\text{sat},z}$) of the fluid flowing through the microchannel and the local wall temperature ($T_{\text{ch},z}$) as follows:

$$h_z = \frac{q_z''}{T_{\text{sat},z} - T_{\text{ch},z}}, \tag{7}$$

where $T_{\text{ch},z}$ is extrapolated from the wall temperature measured on the backside, $T_{w,z}$, by considering the total thermal resistances (R'') of the silicon layer and the thin layer of silicon dioxide:

$$T_{\text{ch},z} = T_{w,z} + q_z'' \times R''. \tag{8}$$

The above equation neglects heat conduction in the axial and lateral directions, as the wall thickness (450 μm) is much smaller than the channel length (35 mm) and the width of the test section (10 mm).

4. Results and Discussion

4.1. Condensation Two-Phase Flow Pattern. Condensation two-phase flow patterns in microchannels have been investigated in many studies. In the literature, five distinct flow regimes have been reported, namely, mist flow, annular flow, injection flow, slug/plug flow, and bubbly flow. In the present study, three flow regimes, from the inlet to the outlet, can be identified: mist/annular flow (Figure 4(a)), injection flow (Figure 4(b)), and slug/bubbly flow (Figure 4(c)) regions. More detailed discussions on the characteristics of condensation two-phase flow pattern in rectangular microchannels with different cross-section designs have been presented in our previous study [14].

Figure 5 presents the occurrence location for the injection flow as a function of steam mass flow rate in the converging microchannel with $\beta = 0.5^\circ$. This figure indicates that the location of the injection flow retreats toward the channel inlet with increasing the coolant flow rate (Q_c) at a given steam mass flow rate or decreasing the steam mass flow rate at a given coolant flow rate. Moreover, the occurrence of injection flow moves to downstream with an increase in the convergence angle at a given coolant flow rate. Such movement of the location of injection flow with mass flow rate and/or convergence angle has a significant effect on the characteristics of condensation heat transfer, which will be discussed in the following sections.

Flow pattern maps are used to determine the flow pattern prevailing under a particular operating condition. Figures 6, 7, and 8 further show the flow pattern maps, constructed in the coordinates of superficial vapor and liquid velocities, that is, j_V and j_L, respectively, observed during experiments in microchannels with different convergence angles. In the present study, flow patterns were observed in four different locations, that is, channel inlet, channel outlet, and locations for void fraction of 0.52 and 0.8 corresponding to the transition boundaries between injection flow and slug/bubbly flow and between mist/annular flow and injection flow, respectively. In the channel inlet region, as shown in the figures, the superficial vapor velocity is the highest and greater than 10 m/s. With a decrease in the void fraction, the superficial vapor velocity decreases while the superficial liquid velocity increases. The transition boundaries that separate the mist/annular flow from the injection flow ($\alpha = 0.8$) and the injection flow from the slug/bubbly flow ($\alpha = 0.52$) are also identified in the figure. Figures 6, 7, and 8 demonstrate that the transition boundaries between mist/annular flow and injection flow and between injection flow and slug/bubbly flow become more instinct as the convergence angle is increased. For these two transition boundaries, the superficial liquid velocity increases very rapidly with an increase in the superficial vapor velocity.

4.2. Condensation Heat Transfer. Figure 9 shows the condensation heat transfer rate as a function of steam mass flow rate in the converging microchannel with $\beta = 0.5^\circ$. This figure clearly demonstrates that the condensation heat transfer rate increases with an increase in the steam mass flow rate at a given coolant flow rate, as reported earlier by Odaymet and Louahlia-Gualous [10], but decreases with an increase in the coolant flow rate at a given steam mass flow rate. The decrease of condensation heat transfer rate with increasing coolant flow rate results primarily from the occurrence location of injection flow moves upstream, as shown previously in Figure 5. This shortens the length of mist/annular flow region and decreases the total condensation heat transfer rate, as the mist/annular flow presents the highest heat transfer compatibility among the three possible flow regimes [15].

To further understand the heat transfer characteristics among microchannels with different convergence angles, the condensation heat fluxes (q_c'') are also examined, as shown in Figure 10(a). Note that in this figure the experimental data of the uniform microchannel ($\beta = 0^\circ$) are from our previous study [15]. This figure shows that at a given coolant flow rate and steam mass flux the condensation heat flux increases with an increase in the convergence angle. This

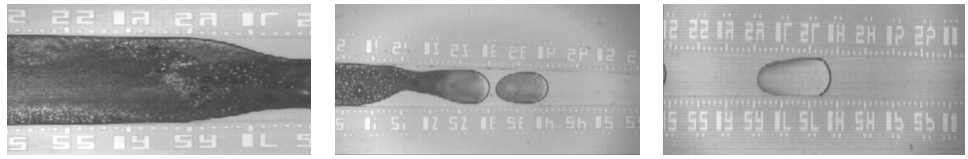

(a) Mist/annular flow (b) Injection flow (c) Slug/bubbly flow

Figure 4: Typical condensation flow patterns in the microchannel.

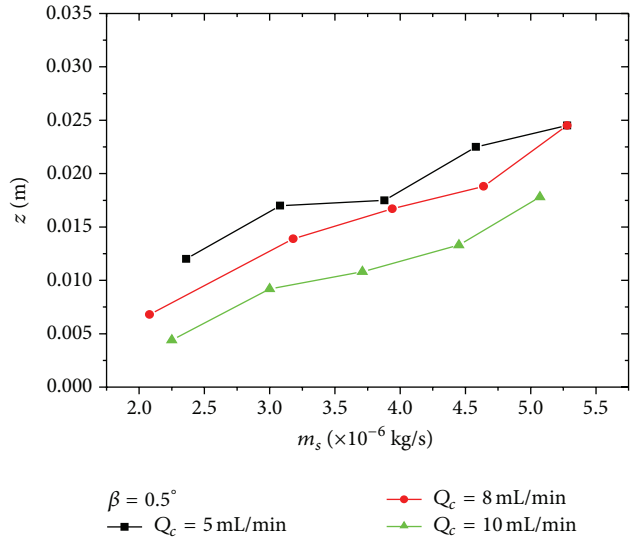

Figure 5: Occurrence location of the injection flow as a function of steam mass flow rate in the microchannel with $\beta = 0.5^{\circ}$.

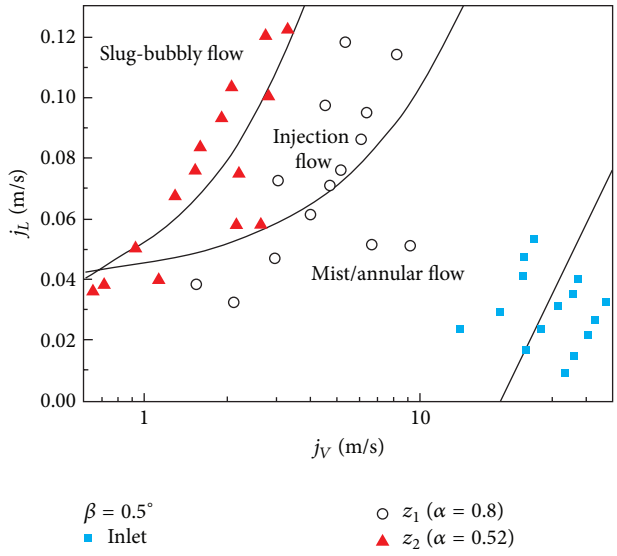

Figure 6: Flow pattern map for the microchannel with $\beta = 0.5^{\circ}$.

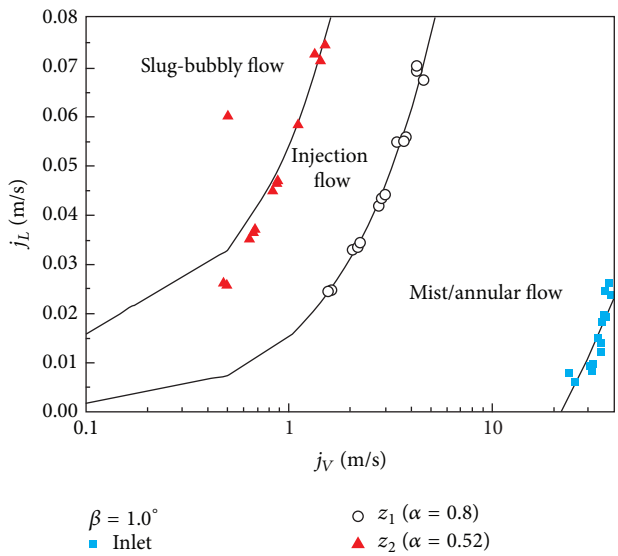

Figure 7: Flow pattern map for the microchannel with $\beta = 1.0^{\circ}$.

is mainly due to the occurrence of injection flow moves to downstream with an increase in the convergence angle, as shown in Figure 10(b). The occurrence of injection flow taking place in a further downstream location indicates that the region of mist/annular flow prevails larger, and, therefore, a much higher bottom heat transfer area for the mist/annular region can be obtained. As the condensation heat transfer rate from the channel is the sum of heat transfer rate from mist/annular flow, injection flow, and bubbly flow regions, that is,

$$q_t = q_1'' A_1 + q_2'' A_2 + q_3'' A_3, \quad (9)$$

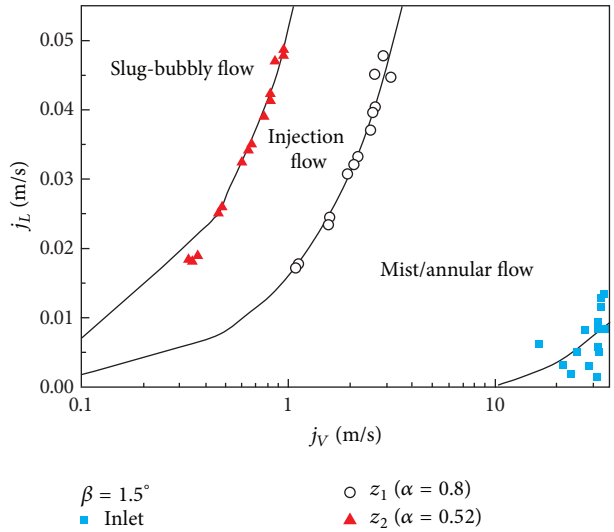

FIGURE 8: Flow pattern map for the microchannel with $\beta = 1.5^\circ$.

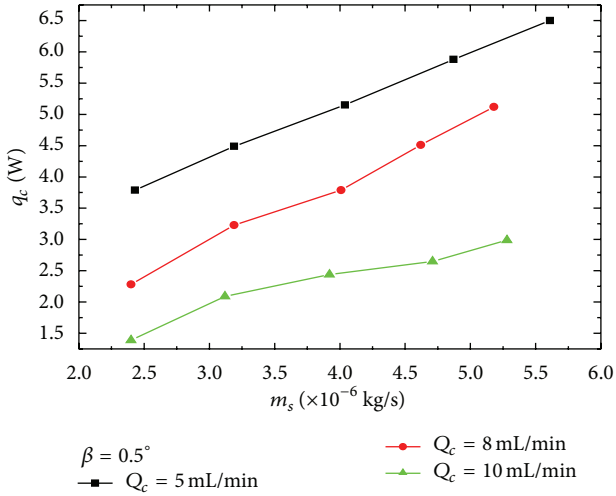

FIGURE 9: Condensation heat transfer rate as a function of steam mass flow rate in the microchannel with $\beta = 0.5^\circ$.

where q_1'', q_2'', and q_3'' are the condensation heat flux from the mist/annular flow, injection flow, and bubbly flow regions, respectively, A_1, A_2, and A_3 are the corresponding heat transfer area for the mist/annular flow, injection flow, and bubbly flow regions, respectively. The heat flux in the mist/annular flow region is much higher than that in the injection flow and bubbly flow regions due to its much thinner liquid film between the vapor and the cooling wall [15]. Consequently, a much higher heat transfer area for the mist/annular flow region will result in a higher total condensation heat transfer rate, as suggested by [10]. Therefore, the mean condensation heat transfer rate is higher for the microchannel with a larger convergence angle.

Figure 11 shows the effect of convergence angle on the local condensation heat transfer coefficient. This figure indicates that, for the microchannel with a given convergence angle, the mist/annular flow region is much higher than

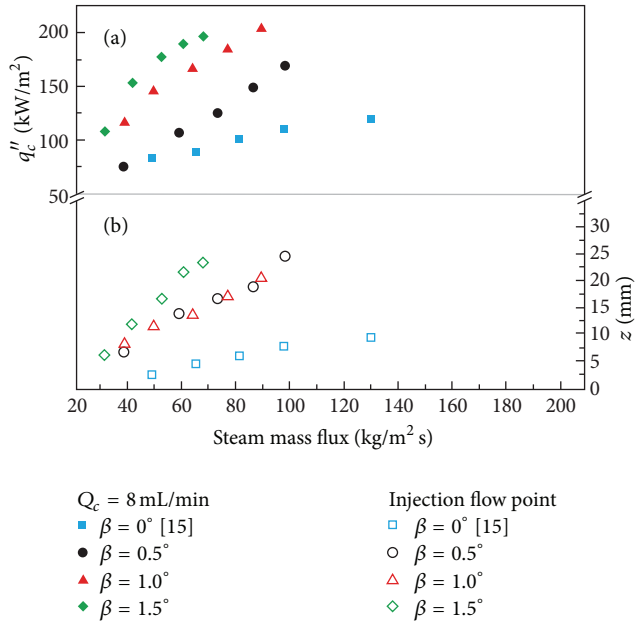

FIGURE 10: (a) Condensation heat flux and (b) injection flow location as a function of steam mass flux for the microchannels with different convergence angles. Data of $\beta = 0^\circ$ are from Kuo and Pan [15].

that in other condensation regimes, as reported by Kuo and Pan [15]. Moreover, for mist/annular flow and injection flow regimes the local condensation heat transfer coefficient decreases generally with an increase in the convergence angle. Interestingly, the uniform microchannel presents a higher heat transfer coefficient in both mist/annular flow and injection flow regions than those in the converging microchannels with convergence angles from 0.5° to 1.5°. As indicated earlier, the injection flow takes place in a much downstream location as the convergence angle increases; much more steam has been condensed in the mist/annular flow region and the liquid film formed may be thicker. Consequently, the local heat transfer coefficient in the mist/annular flow region decreases with an increase in the convergence angle. However, the mean condensation heat flux in the converging microchannel increases with an increase in the convergence angle. This can be understood by rewriting (9) as

$$q_t = h_1 A_1 \left(T_{\text{sat},1} - T_{\text{ch},1}\right) + h_2 A_2 \left(T_{\text{sat},2} - T_{\text{ch},2}\right) + h_3 A_3 \left(T_{\text{sat},3} - T_{\text{ch},3}\right). \quad (10)$$

The condensation heat transfer rate is primarily influenced by the product of heat transfer coefficient and area in the mist/annular flow region. Although the heat transfer coefficient decreases with an increase in the convergence angle, the heat transfer area increases more significantly with an increase in the convergence angle. This explains why the condensation heat transfer rate and, therefore, the mean condensation heat flux increase with an increase in the convergence angle.

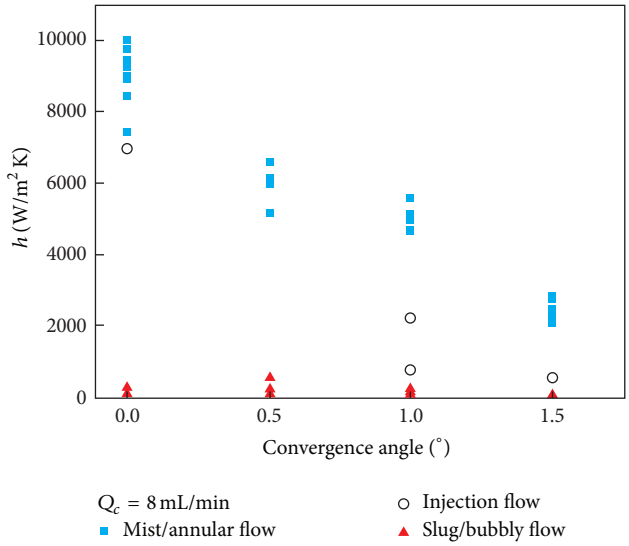

FIGURE 11: Local condensation heat transfer coefficient as a function of convergence angle for different flow regimes. Data of $\beta = 0^\circ$ are from Kuo and Pan [15].

5. Conclusions

This work experimentally investigates the effect of convergence angle of microchannel on two-phase flow and heat transfer during steam condensation. Three convergence angles (0.5°, 1.0°, and 1.5°) of microchannel with the same mean hydraulic diameter of 135 μm are studied. Flow visualization is conducted using a high-speed digital camera. Three condensation regimes, namely, mist/annular flow, injection flow, and slug-bubbly flow can be identified. Flow pattern maps are constructed using coordinates of superficial vapor and liquid velocities, wherein relatively distinct boundaries between the flow patterns are identified. The experimental results show that the condensation heat flux increases with an increase in the convergence angle and/or the steam mass flux at a given coolant flow rate but decreases with an increase in the coolant flow rate at a given steam mass flux. The results further demonstrate that the local condensation heat transfer coefficient in the mist/annular flow region is much higher than that in other condensation regimes. Moreover, the local condensation heat transfer coefficient in the microchannel with a convergence angle of 0.5° is larger than that in the microchannel with the same condensation regime.

Nomenclature

A: Condensation heat transfer area (m^2)
Co: Condensation number (—)
c_p: Specific heat (kJ/kg K)
D_h: Mean hydraulic diameter of a channel (m)
H: Channel depth (m)
h: Heat transfer coefficient (kW/m^2 K)
i_{LV}: Latent heat of vaporization (kJ/kg)
j: Superficial velocity (m/s)
L: Channel length (m)
m_c: Mass flow rate of coolant (kg/s)
m_s: Mass flow rate of steam (kg/s)
q: Condensation heat transfer rate (W)
q'': Condensation heat flux (kW/m^2)
Q_c: Coolant flow rate (mL/min)
R'': Total thermal resistances for conduction through the silicon and silicon dioxide (m^2 K/W)
Re: Reynolds number (—)
T: Temperature (K or °C)
W: Channel width (m)
x: Quality (—)
z: Axial distance from the channel inlet (m).

Greek Symbols

α: Void fraction (—)
β: Convergence angle of a channel (°)
ρ: Density (kg/m^3).

Subscripts

1: Mist/annular flow region
2: Injection flow region
3: Slug/bubbly flow region
c: Coolant or forced convection
ch: Channel
h: Homogeneous
in: Inlet
L: Liquid
out: Outlet
sat: Saturation
t: Total
V: Vapor
w: Wall
z: Distance from channel inlet in the axial direction.

Acknowledgments

This work was supported by the National Science Council of Taiwan under the contract no. NSC 100-2221-E-007-112-MY3, and Ben-Ran Fu would like to express gratitude to Geothermal Technology Department at Industrial Technology Research Institute. This work is reconstructed based on a proceeding paper presented at *the 8th International Symposium on Heat Transfer*, October 21–24, 2012, Beijing, China.

References

[1] H. Y. Wu and P. Cheng, "Condensation flow patterns in silicon microchannels," *International Journal of Heat and Mass Transfer*, vol. 48, no. 11, pp. 2186–2197, 2005.

[2] H. Wu, M. Yu, P. Cheng, and X. Wu, "Injection flow during steam condensation in silicon microchannels," *Journal of*

Micromechanics and Microengineering, vol. 17, no. 8, article 027, pp. 1618–1627, 2007.

[3] X. Quan, P. Cheng, and H. Wu, "Transition from annular flow to plug/slug flow in condensation of steam in microchannels," *International Journal of Heat and Mass Transfer*, vol. 51, no. 3-4, pp. 707–716, 2008.

[4] H. Wu, X. Wu, J. Qu, and M. Yu, "Condensation heat transfer and flow friction in silicon microchannels," *Journal of Micromechanics and Microengineering*, vol. 18, no. 11, Article ID 115024, 2008.

[5] Y. Chen, R. Wu, M. Shi, J. Wu, and G. P. Peterson, "Visualization study of steam condensation in triangular microchannels," *International Journal of Heat and Mass Transfer*, vol. 52, no. 21-22, pp. 5122–5129, 2009.

[6] J. Wu, M. Shi, Y. Chen, and X. Li, "Visualization study of steam condensation in wide rectangular silicon microchannels," *International Journal of Thermal Sciences*, vol. 49, no. 6, pp. 922–930, 2010.

[7] A. Agarwal, T. M. Bandhauer, and S. Garimella, "Measurement and modeling of condensation heat transfer in non-circular microchannels," *International Journal of Refrigeration*, vol. 33, no. 6, pp. 1169–1179, 2010.

[8] X. Ma, X. Fan, Z. Lan, and T. Hao, "Flow patterns and transition characteristics for steam condensation in silicon microchannels," *Journal of Micromechanics and Microengineering*, vol. 21, no. 7, Article ID 075009, 2011.

[9] C. Fang, J. E. Steinbrenner, F.-M. Wang, and K. E. Goodson, "Impact of wall hydrophobicity on condensation flow and heat transfer in silicon microchannels," *Journal of Micromechanics and Microengineering*, vol. 20, no. 4, Article ID 045018, 2010.

[10] A. Odaymet and H. Louahlia-Gualous, "Experimental study of slug flow for condensation in a single square microchannel," *Experimental Thermal and Fluid Science*, vol. 38, pp. 1–13, 2012.

[11] A. Odaymet, H. Louahlia-Gualous, and M. De Labachelerie, "Local heat transfer and flow patterns during condensation in a single silicon microchannel," *Nanoscale and Microscale Thermophysical Engineering*, vol. 16, pp. 220–241, 2012.

[12] S.-M. Kim, J. Kim, and I. Mudawar, "Flow condensation in parallel micro-channels—part 1: experimental results and assessment of pressure drop correlations," *International Journal of Heat and Mass Transfer*, vol. 55, no. 4, pp. 971–983, 2012.

[13] S.-M. Kim and I. Mudawar, "Flow condensation in parallel micro-channels—part 2: heat transfer results and correlation technique," *International Journal of Heat and Mass Transfer*, vol. 55, no. 4, pp. 984–994, 2012.

[14] C. Y. Kuo and C. Pan, "The effect of cross-section design of rectangular microchannels on convective steam condensation," *Journal of Micromechanics and Microengineering*, vol. 19, no. 3, Article ID 035017, 2009.

[15] C. Y. Kuo and C. Pan, "Two-phase flow pressure drop and heat transfer during condensation in microchannels with uniform and converging cross-sections," *Journal of Micromechanics and Microengineering*, vol. 20, no. 9, Article ID 095001, 2010.

[16] J. J. Hwang, F. G. Tseng, and C. Pan, "Ethanol-CO_2 two-phase flow in diverging and converging microchannels," *International Journal of Multiphase Flow*, vol. 31, no. 5, pp. 548–570, 2005.

[17] R. J. Moffat, "Describing the uncertainties in experimental results," *Experimental Thermal and Fluid Science*, vol. 1, no. 1, pp. 3–17, 1988.

[18] B. R. Fu, F. G. Tseng, and C. Pan, "Two-phase flow in converging and diverging microchannels with CO_2 bubbles produced by chemical reactions," *International Journal of Heat and Mass Transfer*, vol. 50, no. 1-2, pp. 1–14, 2007.

[19] A. Kawahara, P.-Y. Chung, and M. Kawaji, "Investigation of two-phase flow pattern, void fraction and pressure drop in a microchannel," *International Journal of Multiphase Flow*, vol. 28, no. 9, pp. 1411–1435, 2002.

Hindawi Publishing Corporation
Advances in Mechanical Engineering
Volume 2013, Article ID 181856, 8 pages
http://dx.doi.org/10.1155/2013/181856

Research Article

Computational Analysis of Droplet Mass and Size Effect on Mist/Air Impingement Cooling Performance

Zhenglei Yu, Tao Xu, Junlou Li, Tianshuang Xu, and Tatsuo Yoshino

College of Mechanical Science & Engineering, Jilin University, Changchun 130025, China

Correspondence should be addressed to Tatsuo Yoshino; yoshinojlu@sina.com

Received 14 June 2013; Accepted 20 August 2013

Academic Editor: Godson Asirvatham Lazarus

Impingement cooling has been widely employed to cool gas turbine hot components such as combustor liners, combustor transition pieces, turbine vanes, and blades. A promising technology is proposed to enhance impingement cooling with water droplets injection. However, previous studies were conducted on blade shower head film cooling, and less attention was given to the transition piece cooling. As a continuous effort to develop a realistic mist impingement cooling scheme, this paper focuses on simulating mist impingement cooling under typical gas turbine operating conditions of high temperature and pressure in a double chamber model. Furthermore, the paper presents the effect of cooling effectiveness by changing the mass and size of the droplets. Based on the heat-mass transfer analogy, the results of these experiments prove that the mass of $3E-3$ kg/s droplets with diameters of 5–35 μm could enhance 90% cooling effectiveness and reduce 122 K of wall temperature. The results of this paper can provide guidance for corresponding experiments and serve as the qualification reference for future more complicated studies with convex surface cooling.

1. Introduction

Efficiency is one of the most important parameters in evaluating the performance of a gas turbine engine. With even a 1% efficiency increase, the operating costs can be substantially reduced over the life of a typical power plant. One of the most effective ways to improve the gas turbine system efficiency is to increase the combustor outlet temperature. A higher outlet temperature leads to better system thermodynamic efficiency. However, outlet temperature is limited by the highest temperature that the material of the gas turbine can withstand. Spontaneously, we need to consider the efficiency of cooling technology which plays a significant role in the whole process as the more efficiency it applied, the higher temperature of combustor could exit and the efficiency of gas turbine cycle could reach. Cooling technology has been successfully applied in protecting turbine airfoils from high temperature since the last half century [1, 2]. The majority of the literature has been covered in the book by Han et al. [3]. Such that most of these studies concentrate on blade shower head film cooling; however, less attention is given to the transform piece cooling [4]. As one of most important cooling technology, impingement cooling has been studied on transform piece cooling.

The early investigation on impingement cooling has been summarized by Chupp et al. [5]. They did experimental study on impingement of a single row of circular jets on semicircular concave surface. Their results suggested general increases in heat transfer with approximately the 0.7 power of jet Reynolds number. Dyban and Mazur [6] measured heat transfer coefficient on a parabolic concave surface and investigated the effect of jet flow passage curvature. McCormack et al. [7] found that Nusselt numbers were increased by 100–150% on the concave surface. Hrycak [8] proposed correlations for stagnation and average heat transfer coefficient for a row of impinging jets on a cylindrical concave surface. Wei et al. [9] investigated impingement and serpentine convection cooling under the effect of rotation. Their results suggested that rotation effects increase the serpentine cooling and reduce the jet impingement cooling.

As the working gas temperature continuously increases to augment thermal efficiency, new cooling techniques are needed to surpass incremental improvements of conventional gas turbine cooling technologies. A promising technology is to enhance film cooling with mist (small water droplets) injection. Based on the aforementioned heat transfer mechanisms, mist can be used in gas turbine systems in different

ways, including gas turbine inlet air fog cooling [10], overspray cooling through wet compression in the compressor [11], and airfoils (vanes and blades) internal cooling [12–16]. Recently, Li and Wang [17] conducted the first numerical simulations of air/mist film cooling. They showed that injecting a small amount of droplets (2% of the coolant flow rate) could enhance the cooling effectiveness about 30–50%. Li and Wang [18] continued a more fundamental study on investigating the effect of various models on the computational results including the turbulence models, dispersed phase modeling, different forces models (Saffman, thermophoresis, and Brownian), trajectory tracking model, near-wall grid arrangement, and mist injection scheme.

As a continuous effort to develop a realistic impingement cooling scheme, this paper focuses on using a promising technology to enhance impingement cooling which is to inject water mist into the coolant flow. The main objective of this thesis is to elucidate how the mass and dimension of the droplet affect the mist impingement cooling performance over a curved surface with a hole of double chamber model, calculated by CFD. Earlier studies discussed the mist film performance on the blade and combustor of gas turbine [10–15]. The model created in the paper looks like a flat with two double chambers, simulating the structure of transition piece. Accordingly, the main objectives of the investigation are as follow: (1) model establishment: discrete-hole impingement cooling flat surface with an injection coolant intercalation; (2) model analysis: the droplet mass ratio and dimension on mist impingement cooling effectiveness over a flat surface; (3) results comparison: the temperature of inner wall, film cooling effectiveness, velocity magnitude contours, and droplet particle track in various conditions. The results of this paper can serve as a reference for future experimental validation and technical implementation to real gas turbine applications.

2. Numerical Method

The new transition piece features a rounded body shape that balances the heat transfer loading both internally and externally and eliminates resonant frequency concerns [19], which consists of heavier walls, single-piece aft ends, ribs, seal arrangements, and selective cooling. It has an upstream aperture for the gas flow (which is cylindrical), and it is used to receive the gas flow directly from the corresponding combustion liners with a high level of enthalpy; transition pieces are conjured in a longitudinal direction so that their downstream ends comprise arched segments to form a ring-type configuration which opens toward the first stage of the gas turbine (stator) [20, 21].

A schematic of the flow domain along with boundary conditions and dimensions is given in Figure 1. As shown in the figure, the flat model has two chambers with length of 1050 mm, and the outer and inner height is 38 mm and 162 mm, respectively. The outer chamber in Figure 1 is called coolant chamber as the side is closed. Contrarily, the inner chamber goes by the name of mainstream chamber as the gas could pass through it from one side to another. There is a hole on the surface of the outer wall, and the distance from the hole to the end of the model is 520 mm. The size of all the holes is about 10.26 mm.

2.1. Turbulence Model (Realizable k-ε). The present film cooling study involves flow which is steadied, Newtonian, three-dimensional, incompressible, and turbulent. Such flow behaves according to three fundamental laws, namely, the laws of continuity, conservation of momentum, and conservation of energy.

The realizable k-ε model proposed by Shih et al. [22] was intended to address these deficiencies of standard k-ε models by adopting the following: (1) realizable k-ε model contains a new formulation for the turbulent viscosity; and (2) a new transport equation for the dissipation rate, ε, is derived from an exact equation for the transport of the mean square velocity fluctuation. The modeled transport equations for k and ε in the realizable k-ε model are

$$\frac{\partial}{\partial x_i}(\rho k u_i) = \frac{\partial}{\partial x_j}\left[\left(\mu + \frac{\mu_t}{\sigma_k}\right)\frac{\partial k}{\partial x_j}\right] + G_k + G_b - \rho\varepsilon - Y_M + S_k,$$

$$\frac{\partial}{\partial x_i}(\rho \varepsilon u_i) = \frac{\partial}{\partial x_j}\left[\left(\mu + \frac{\mu_t}{\sigma_\varepsilon}\right)\frac{\partial \varepsilon}{\partial x_j}\right] + \rho C_1 S_\varepsilon - \rho C_2 \frac{\varepsilon^2}{k + \sqrt{\nu\varepsilon}} - C_{1\varepsilon}\frac{\varepsilon}{k}C_{3\varepsilon}G_b + S_\varepsilon, \tag{1}$$

where

$$C_1 = \max\left[0.43, \frac{\eta}{\eta + 5}\right], \quad \eta = S\frac{\varepsilon}{k}, \quad S = \sqrt{2S_{ij}S_{ij}}. \tag{2}$$

In these equations, G_k and G_b represent the generation of turbulent kinetic energy due to the mean velocity gradients and buoyancy, respectively. Y_M is the contribution of the fluctuating dilatation in compressible turbulence to the overall dissipation rate, and $C_{1\varepsilon}$ and C_2 are constants. S_k and S_ε are user-defined source terms. The turbulent (or eddy) viscosity μ_t is computed by combining k and ε as follows:

$$\mu_t = \frac{\rho C_\mu k^2}{\varepsilon}. \tag{3}$$

A benefit of the realizable k-ε model is that it better predicts the spreading rate of both planar and round jets. It is also stated that it has superior performance for flows involving rotation, separation, recirculation, and boundary layers under adverse pressure gradients.

2.2. Stochastic Particle Tracking. To track the trajectory of droplets, the hydrodynamic drag, gravity, and forces such as the "virtual mass" force, thermophoretic force, Brownian force, and Saffman's lift force are combined to accelerate the droplet. The energy equation for any individual droplet can be given as the following equation:

$$m_p c_p \frac{dT}{dt} = \pi d^2 h\left(T_\infty - T\right) + \frac{dm_p}{dt}h_{fg}, \tag{4}$$

where h_{fg} is the latent heat. The convective heat transfer coefficient (h) can be obtained with an empirical correlation [23, 24].

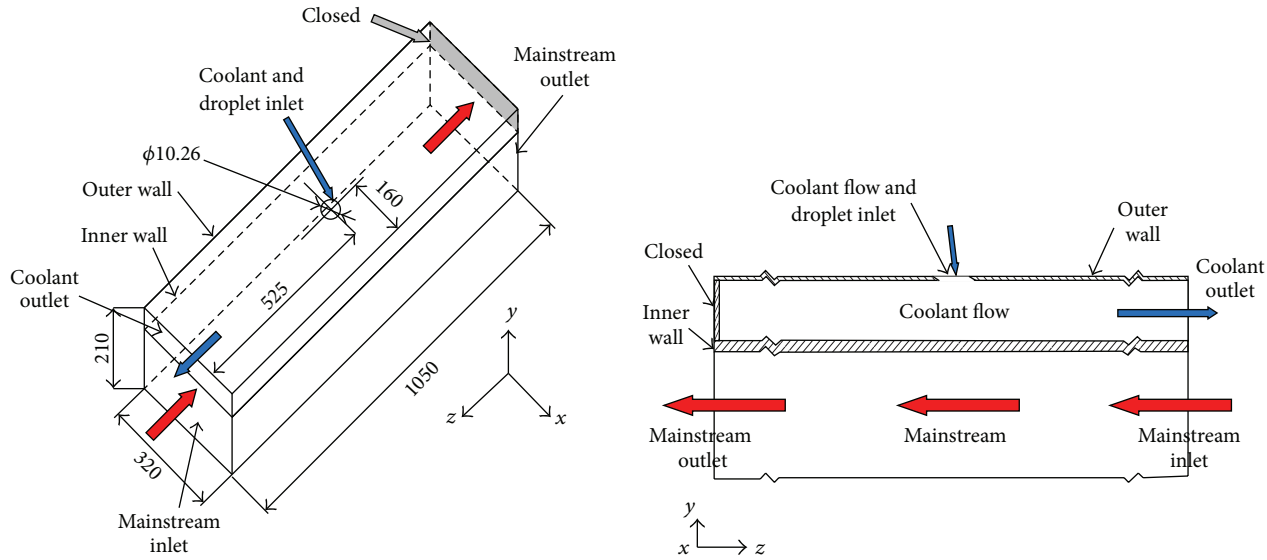

FIGURE 1: Computational domain showing boundary conditions.

The mass change rate or vaporization rate in (4) is governed by concentration difference between droplet surface and the air stream:

$$-\frac{dm_p}{dt} = \pi d^2 k_c \left(C_s - C_\infty\right), \tag{5}$$

where k_c is the mass transfer coefficient and C_s is the vapor concentration at the droplet surface, which is evaluated by assuming that the flow over the surface is saturated. C_∞ is the vapor concentration of the bulk flow, obtained by solving the transport equations. When the droplet temperature reaches the boiling point, the following equation can be used to evaluate its evaporation rate [25]:

$$-\frac{dm_p}{dt} = \pi d^2 \left(\frac{\lambda}{d}\right)\left(2.0 + 0.46\mathrm{Re}_d^{0.5}\right) \times \frac{\ln\left(1 + c_p\left(T_\infty - T\right)/h_{fg}\right)}{c_p}, \tag{6}$$

where λ is the gas/air heat conductivity and c_p is the specific heat of the bulk flow.

Stochastic method [26] is used to consider turbulence dispersion effect on droplets tracking. The droplet trajectories are calculated with the instantaneous flow velocity $(\overline{u} + u')$, and the velocity fluctuations are then given as

$$u' = \varsigma\left(\overline{u'^2}\right)^{0.5} = \varsigma\left(\frac{2k}{3}\right)^{0.5}, \tag{7}$$

where ς is a normally distributed random number. This velocity will apply during the characteristic lifetime of the eddy (t_e), a time scale calculated from the turbulence kinetic energy, and dissipation rate. After this time period, the instantaneous velocity will be updated with a new ς value until a full trajectory is obtained.

2.3. Boundary Conditions. Boundary conditions were applied to specific faces within the domain to specify the flow and thermal variables that dictate conditions within the model. They are a critical constituent to the simulation, and it is important that they are specified appropriately. The masses of water droplets are 0, $3E-6$, $3E-5$, $3E-4$, and $3E-3$ kg/s. The droplet size is given as 5, 15, 25, 35, 45, and 55 μm.

Figure 1(a) also shows the boundary conditions used for the modeling. Respectively, the cooling air and gas are coursing along the cooling chamber and the mainstream chamber with the opposite direction. In the cooling chamber, the simulation is performed using air as the cooling flow; velocity and temperature contours are set on the jet holes, and then out from the exit mouth. In another chamber, assume that the mainstream is a mixture of O_2, H_2O, CO_2, N_2, and some rare gas. Gas velocity and temperature contours are set on the surface of the sector section; pressure on the exit mouth and natural convection on the outside wall of the model are considered as boundary condition (Table 1) [4]. In gas chamber, egress of the mainstream was fixed and exported free expansion. The assumption of the solid wall of the quarter torus is modeled with a hypothesis of negligible thermal resistance by conduction; the thermal properties of the material were considered by Nimonic 263. The temperature of the coolant and mainstream flow are set as 300 K and 1300 K, respectively.

2.4. Mesh and Simulation Procedures. The computational domain incorporates the model, the HEXA mesh in the software, ICEM/CFD, used to generate the structured multiblock and the body-fitted grid system. This software allows to separate grids generated for different parts of the flow domain, using an appropriate grid system. In this study, the grid system associated with the parts of the mainstream and the coolant supply plenum is H-type. Figure 2 shows the grids

Table 1: Boundary conditions.

Component	Boundary conditions	Magnitude
Mainstream inlet	Mass flux rate	31.46 [kg/s]
	Gas temperature	1300 [K]
	Turbulent intensity	5 [%]
	Hydraulic diameter	0.324 [m]
Mainstream outlet	Pressure	1.512 [MPa]
	Turbulent intensity	5 [%]
	Hydraulic diameter	0.324 [m]
	Convection coefficient	10 [W/m^{2}K]
Coolant chamber	Air temperature	300 [K]
	Pressure	1.4552 [MPa]
	Pressure recovery coefficient	0.95
	Turbulent intensity	5 [%]
	Hydraulic diameter	0.01026 [m]
Droplet	Velocity	0 [m/s]
	Mass	$3E-3$, $3E-4$, $3E-5$, and $3E-6$ [kg/s]
	Size	5, 10, 15, 20, 50, and 75 [μm]

of the computational domain. The total number of the cells for the 3D domain is 198,068.

This study uses a commercial CFD code based on the control-volume method, ANSYS-FLUENT 12.0.16, which in order to predict temperature, cooling effectiveness, velocity fields, and droplet particle track at different droplet mass and size. All runs were made on a PC cluster with four Pentium-4 2.8 GHz personal computers. The convergence criteria of the steady-state solution are judged by the reduction in the mass residual by a factor of 6, typically, in 2000 iterations.

3. Result and Discussion

In this section, the results obtained with a different mass ratio and dimension of droplet are presented in order to validate the CFD model above so that the mist impingement cooling physics would be well studied.

3.1. Effect of Droplet Mass. Comparison of the temperature and cooling effectiveness results of four droplet masses ($3E-3$, $3E-4$, $3E-5$, and $3E-6$ kg/s) is shown in Figure 3. In this condition, the size of all droplets is 5 μm. Similar to the results under high pressure and temperature conditions [4], the heavier droplets are shown to provide better enhancements. The figure illustrates that the temperature at the starting point of the wall is high, and then it starts to go down. The starting point is cooled by the coolant holes at the $Z = 525$ mm on the outer wall, while the same temperature is maintained throughout the coolant hole. With the droplet mass increase, the color of temperature distribution in the same region becomes lighter which indicates that the surface has been better protected by the coolant flow. Since the jet flow seems to possess sufficient capacity to receive more mist flow, it is interesting to see the effect of injecting more mist into the jet flow.

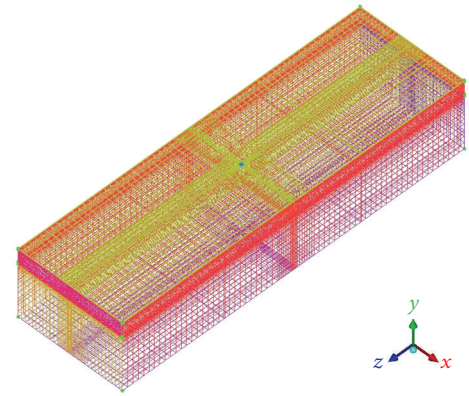

Figure 2: Mesh.

The adiabatic cooling effectiveness (η) is used to examine the performance of film cooling. The definition of η is

$$\eta = \frac{T_g - T_{\text{aw}}}{T_m - T_c}, \tag{8}$$

where T_g is the mainstream hot gas inlet temperature, which is a fixed value for calculation of the adiabatic cooling effectiveness of any location, and T_c is the temperature of the coolant, which is assigned as a constant of 300 K in this issue. T_{aw} is the adiabatic wall temperature.

The cooling effectiveness is defined the same as it was in the previous section. To evaluate the cooling enhancement of adding mist into the air film, the net enhancement is plotted on the secondary y-axis on the right-hand side. The net enhancement is defined as follows:

$$\text{Net Enhancement} = \frac{(\eta_m - \eta)}{\eta}. \tag{9}$$

The subscript "m" means mist is added. Without any subscript, it means air-only film is used. From the definition, net enhancement is zero if the mist cooling effectiveness is the same as the air-only cooling effectiveness. Note that mist film cooling itself can be improved by using different droplet masses. Figure 4 shows the cooling effectiveness and enhancement ratio when different droplet masses are employed. For simplicity, it can be seen that when the droplet mass is $3E-6$ kg/s, the adiabatic cooling effectiveness increases significantly. Compared with the normal case, the cooling effectiveness of MIC provides 90% in axis $Z = 550$ mm. The cooling effectiveness lines are almost the same with no MIC case condition when the droplet mass is $3E-6$, $3E-5$, and $3E-4$ kg/s. Therefore, it is plausible that the temperature and cooling effectiveness contours of lighter mass cases ($3E-6$, $3E-5$, and $3E-4$ kg/s) are similar to the no MIC case.

3.2. Effect of Droplet Size. In real applications, the size of droplet is another factor that could affect the mist impingement cooling results. Comparison of the cooling effectiveness

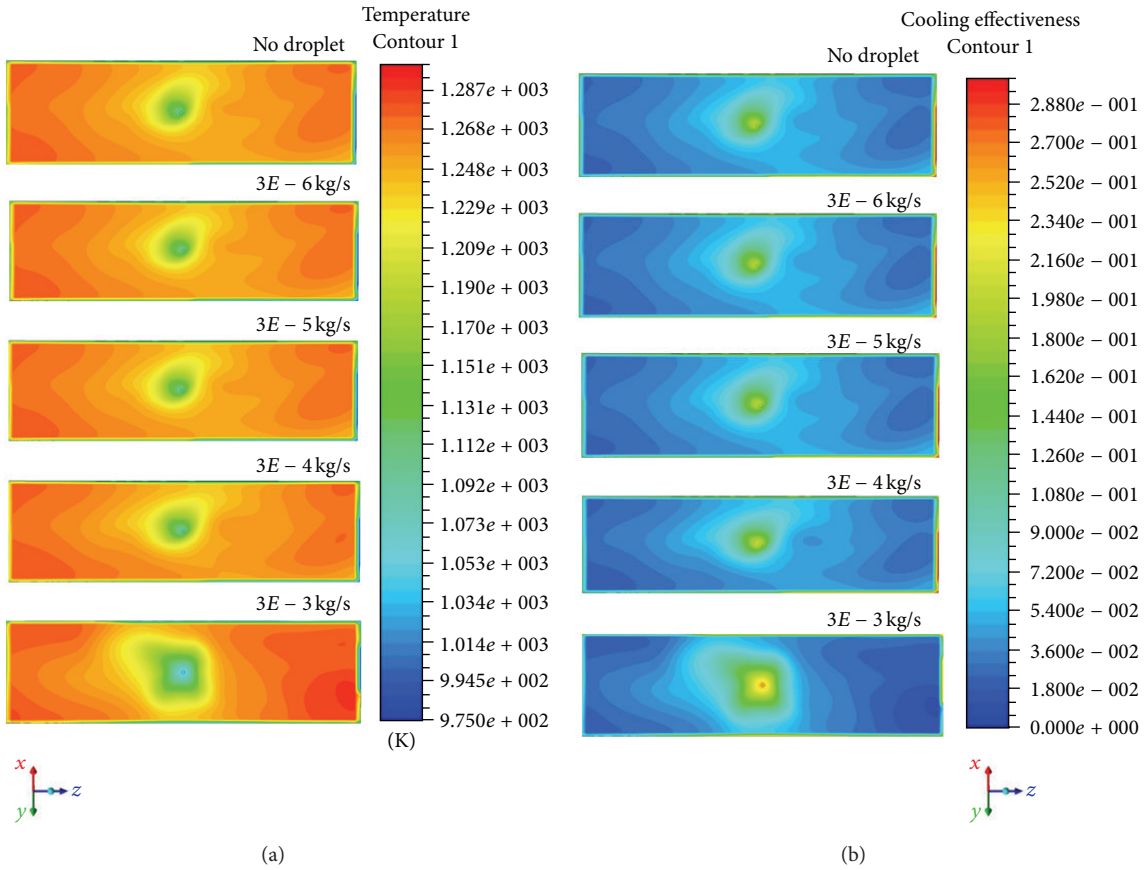

Figure 3: Comparative analysis of temperature and cooling effectiveness at different droplet masses (no droplet, $3E-6$, $3E-5$, $3E-4$, and $3E-3$ kg/s) showing vortex induction towards the inner wall and (a) temperature distribution of inner wall and (b) cooling effectiveness distribution.

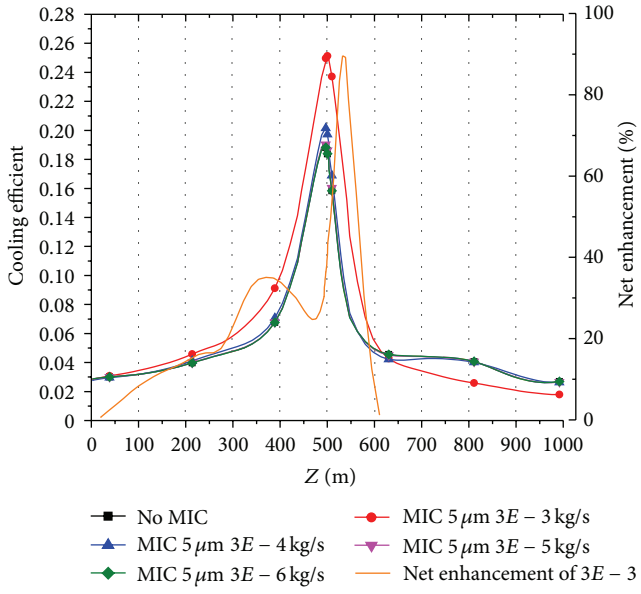

Figure 4: Distributions of averaged cooling effectiveness and net enhancement of $3E-3$ kg/s in the different droplet masses.

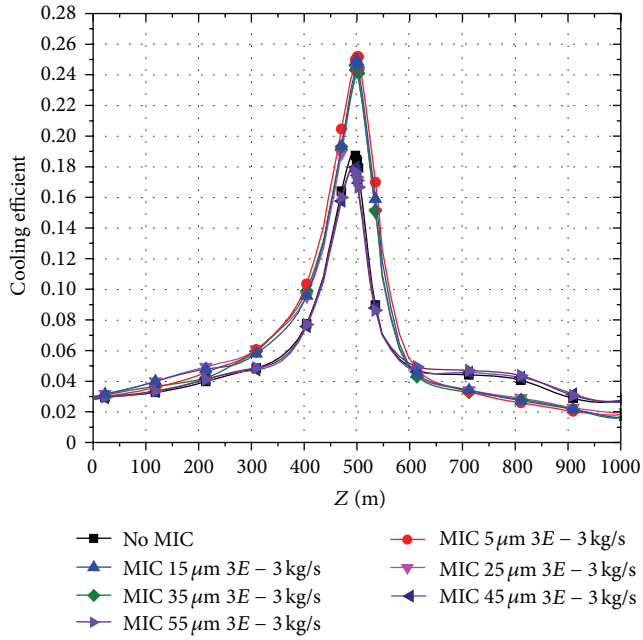

Figure 5: Distributions of averaged cooling effectiveness in different sizes with $3E-3$ kg/s droplet mass.

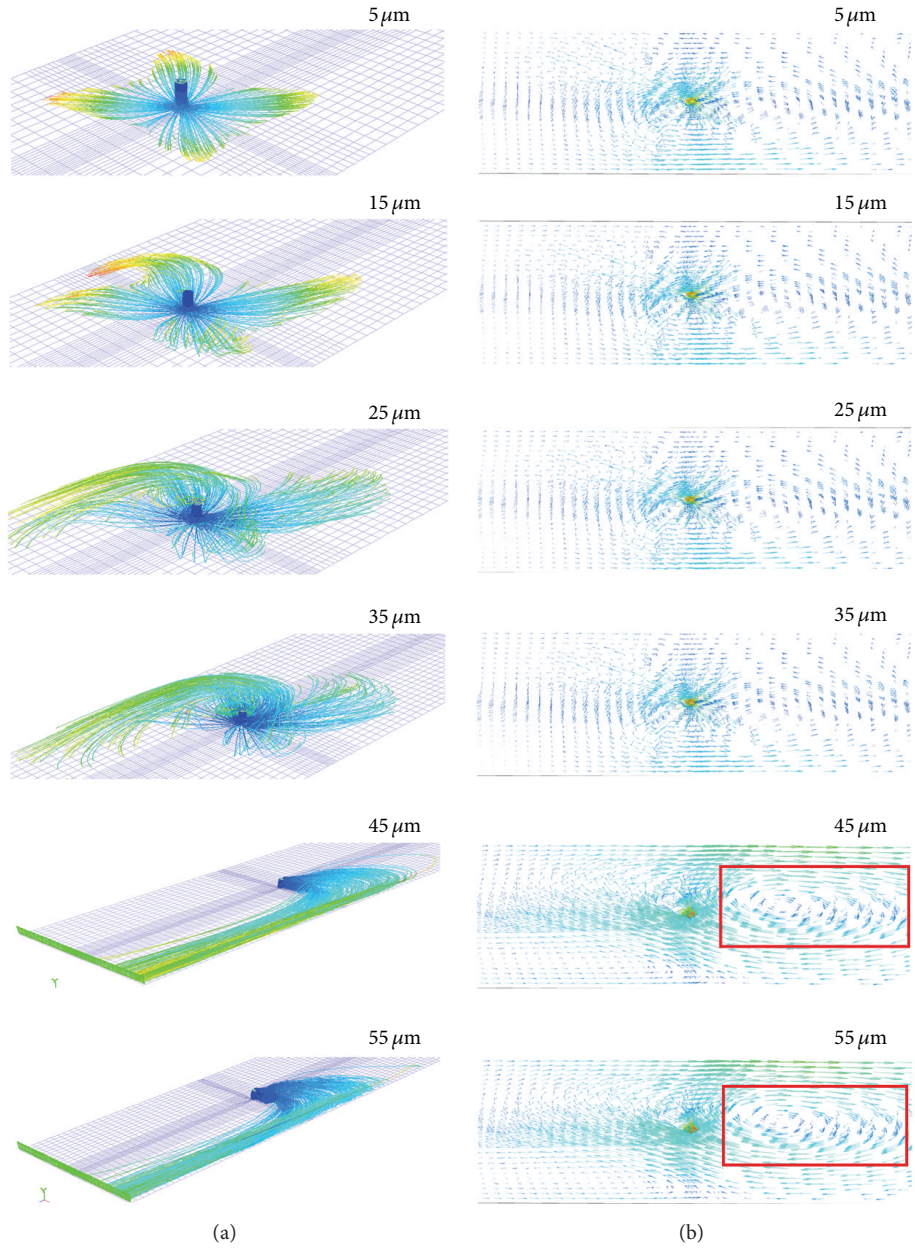

Figure 6: Distributions of velocity magnitude contours and droplet particle track in different sizes with $3E-3$ kg/s droplet mass: (a) droplet particle track and (b) velocity vector plot.

in different sizes (5, 15, 25, 35, 45, and 55 μm) with $3E-3$ kg/s droplet mass is shown in Figure 5. In the picture, the cooling effectiveness lines are almost the same when the droplet size is 5, 15, 25, and 35 μm. However, the cooling effectiveness is reduced by increasing the droplet size (45 and 55 μm), and they all have the same trend with the normal case. Before axis $Z = 600$ mm, the smaller droplets are shown to provide better enhancements. The small droplets provide higher surface to volume ratio, so evaporation completes more rapidly and effectively than the larger droplets. The results show that its effect on cooling effectiveness is negligible because the size is found very large (larger than 35 μm) in the currently studied cases.

Figure 6 shows the velocity magnitude contours and the droplet particle track in the different size cases. Figure 6(a) shows that the droplets impact the inner wall, which moved with the coolant jet from the hole. In the small size cases (5, 15, 25, and 35 μm) of Figure 6(a), all the droplets evaporate before axis $Z = 600\,\mu$m in the coolant chamber. However, larger droplets may exit the computational domain without complete evaporation due to low evaporation rate or short residential time. Therefore, it is plausible that the large droplets move farther away from the wall than small droplets under the condition in the current study due to the high inertia force from jet injection. This mechanism of larger droplets moving further away from the wall contributes to

ineffectiveness of producing film cooling protection of the inner wall even though the latent heat absorption can reduce the coolant chamber temperature.

To explain the effect of droplet size on MIC enhancement with flat configuration, velocity vectors at the coolant chamber are plotted and shown in Figure 6(b). The figure shows that the small size cases (5, 15, 25, and 35 μm) jet velocity vectors are much shorter in the coolant chamber than large size cases (45 and 55 μm). The small size cases jet is formed as the impinging jet turning parallel to the surface from the stagnation region. Due to jet-to-jet interaction after impingement, the flow becomes complex with a large 3D recirculation zone in the large size cases. Corresponding to the large recirculation zone, the droplet particle track of the large size cases offsets to one side of coolant chamber.

4. Conclusion

A complete three-dimensional numerical simulation of a mist impingement cooled flat double chamber model is conducted to study coolant structure, and it has been proven that this structure could be influenced by the droplet mass and size. This feature is very favorable in considering applying mist impingement cooling in the transition piece because of the following.

(i) The liquid droplets in the film provide a more extended impingement cooling coverage effect than the air impingement cooling.

(ii) Compared with no MIC case, the maximum enhancement of adiabatic cooling effectiveness is about 90% for the $3E-3$ kg/s droplet mass case, corresponding to an additional adiabatic wall temperature reduction of 122 K.

(iii) Smaller size droplets (5, 15, 25, and 35 μm) provide 80–90% better cooling performance than larger size droplets (45 and 55 μm).

Nomenclature

D_a: Diameter of coolant chamber
D_g: Diameter of mainstream chamber
L: Length of the model
T: Absolute static temperature
X, Y, Z: Nondimensional coordinates in diameter, spanwise, and mainstream directions.

Greek Symbols

α: Injection angle
η: Film cooling effectiveness.

Suffixes

g: Mainstream flow
c: Coolant flow
aw: Adiabatic wall
m: Mist added
s: Size.

Conflict of Interests

The authors declare that they have no conflict of interests.

Acknowledgments

This research is supported by the Technology Development of Jilin Province (no. 20126001), Key Technologies R&D Program of Changchun (no. 10KZ03), and the National Natural Science Foundation of China (no. 51205159).

References

[1] R. J. Goldstein, *Advances in Heat Transfer*, Academic Press, New York, USA, 1971.

[2] R. J. Margason, "Fifty years of jet in cross-flow research," *Computational and Experimental Assessment of Jets in Cross Flow*, vol. 41, pp. 7–34, 1993.

[3] J. C. Han, S. Dutta, and S. V. Ekkad, *Gas Turbine Heat Transfer and Cooling Technology*, Taylor and Francis, New York, USA, 2000.

[4] Z. L. Yu, T. Xu, J. L. Li, L. Ma, and T. S. Xu, "Comparison of a series of double chamber model with various hole angles for enhancing cooling effectiveness," *International Communications in Heat and Mass Transfer*, vol. 44, pp. 38–44, 2013.

[5] R. E. Chupp, H. E. Helms, P. W. McFadden, and T. R. Brown, "Evaluation of internal heat transfer coefficients for impingement cooled turbine airfoils," *Journal of Aircraft*, vol. 6, pp. 203–208, 1969.

[6] Y. P. Dyban and A. I. Mazur, "Heat transfer from a flat air jet flowing into a concave surface," *Heat Transfer*, vol. 2, pp. 15–22, 1970.

[7] P. D. McCormack, H. Welker, and M. Keeleher, "Taylor-Goertler vortices and their effect on heat transfer," *ASME Journal of Heat Transfer*, vol. 92, pp. 101–112, 1970.

[8] P. Hrycak, "Heat transfer from a row of impinging jets to concave cylindrical surfaces," *International Journal of Heat and Mass Transfer*, vol. 24, no. 3, pp. 407–419, 1981.

[9] H. Wei, D. Chiang, and H. L. Li, "Jet impingement and forced convection cooling experimental study in rotating turbine blades," in *Proceedings of the ASME Turbo Expo 2000 (GT '00)*, Paper No. GT2009-59795, Munich, Germany, May 2000.

[10] M. Chaker, C. B. Meher-Homji, and T. Mee, "Inlet fogging of gas turbine engines, part A: fog droplet thermodynamics, heat transfer and practical considerations," in *Proceedings of the ASME Turbo Expo 2002 (GT '02)*, pp. 413–428, Amsterdam, The Netherlands, June 2002.

[11] V. Petr, "Analysis of wet compression in GT's," in *Proceedings of the International Conference on Energy and the Environment (ICEE '03)*, vol. 1, pp. 489–494, Shanghai, China, December 2003.

[12] T. Guo, T. Wang, and J. L. Gaddis, "Mist/steam cooling in a heated horizontal tube, part 1: experimental system, part 2: results and modeling," *ASME Journal of Turbomachinery*, vol. 122, no. 2, pp. 360–374, 2000.

[13] T. Guo, T. Wang, and J. L. Gaddis, "Mist/steam cooling in a 180-degree tube bend," *ASME Journal of Heat Transfer*, vol. 122, no. 4, pp. 749–756, 2000.

[14] X. Li, J. L. Gaddis, and T. Wang, "Mist/steam cooling by a row of impinging jets," *International Journal of Heat and Mass Transfer*, vol. 46, no. 12, pp. 2279–2290, 2003.

[15] X. Li, J. L. Gaddis, and T. Wang, "Mist/steam heat transfer with jet impingement onto a concave surface," *ASME Journal of Heat Transfer*, vol. 125, no. 3, pp. 438–446, 2003.

[16] T. Wang and X. Li, "Mist film cooling simulation at gas turbine operating conditions," *International Journal of Heat and Mass Transfer*, vol. 51, no. 21-22, pp. 5305–5317, 2008.

[17] X. Li and T. Wang, "Simulation of film cooling enhancement with mist injection," *ASME Journal of Heat Transfer*, vol. 128, no. 6, pp. 509–519, 2006.

[18] X. Li and T. Wang, "Effects of various modeling on mist film cooling," *ASME Journal of Heat Transfer*, vol. 129, no. 4, pp. 472–482, 2007.

[19] J. Benoit, C. Johnston, and M. Zingg, "Enhancing gas turbine power plant profitability: chronic transition piece and turbine part failures in some 501F gas turbines led to a replacement part redesign," *Power Engineering*, vol. 111, no. 11, pp. 140–144, 2007.

[20] J. A. Alfaro-Ayala, A. Gallegos-Muñoz, and Z. A. Alejandro, "Thermal and fluid dynamic analysis of the gas turbine transition piece," in *Proceedings of the ASME Turbo Expo 2009: Power for Land, Sea, and Air (GT '09)*, pp. 1387–1396, ASME, Orlando, Fla, USA, June 2009.

[21] A. Gallegos Muñoz, V. Ayala-Ramírez, J. A. Alfaro-Ayala, and B. M. T. Acosta, "Optimization of the transition piece applying genetic algorithms," *Applied Thermal Engineering*, vol. 31, no. 16, pp. 3214–3225, 2011.

[22] T. Shih, W. W. Liou, A. Shabbir, Z. Yang, and J. Zhu, "A new κ-ε eddy viscosity model for high reynolds number turbulent flows," *Computers and Fluids*, vol. 24, no. 3, pp. 227–238, 1995.

[23] W. E. Ranz and W. R. Marshall Jr., "Evaporation from drops, part I," *Chemical Engineering Progress*, vol. 48, pp. 141–146, 1952.

[24] W. E. Ranz and W. R. Marshall Jr., "Evaporation from drops, part II," *Chemical Engineering Progress*, vol. 48, pp. 173–180, 1952.

[25] K. Y. Kuo, *Principles of Combustion*, John Wiley and Sons, New York, NY, USA, 1986.

[26] ANSYS FLUENT 12. 1 Documentation, ANSYS Inc.

Hindawi Publishing Corporation
Advances in Mechanical Engineering
Volume 2013, Article ID 270159, 6 pages
http://dx.doi.org/10.1155/2013/270159

Research Article

Economic Analysis for Rebuilding of an Aged Pulverized Coal-Fired Boiler with a New Boiler in an Aged Thermal Power Plant

Burhanettin Cetin and Merve Abacioglu

Mechanical Engineering Department, Yildiz Technical University, 34349 Istanbul, Turkey

Correspondence should be addressed to Burhanettin Cetin; cetin@yildiz.edu.tr

Received 25 March 2013; Revised 27 May 2013; Accepted 24 June 2013

Academic Editor: Ahmet Selim Dalkılıç

Fossil-fired thermal power plants (TPP) produce a significant part of electricity in the world. Because of the aging TPPs and so their equipment (especially boiler), thermal power plants also produce less power than their installed capacities, and there has been power loss in time. This situation affects the supply and demand balance of countries. For this reason, aging equipments such as pulverized coal-fired boiler (PCB) must be renewed and power loss must be recovered, instead of building new TPPs. In this study, economic analysis of rebuilding an aged pulverized coal-fired boiler with a new pulverized coal-fired boiler including flue gas desulfurization (FGD) unit and a circulating fluidized bed boiler (FBB) are investigated in an existing old TPP. Emission costs are also added to model, and the developed model is applied to a 200 MWe pulverized coal-fired thermal power plant in Turkey. As a result, the payback period and the net present value are calculated for different technical and economic parameters such as power loss, load factor, electricity price, discount rate, and escalation rate by using the annual value method. The outcomes of this study show that rebuilding of a pulverized coal-fired boiler with a new one is amortized itself in a very short time.

1. Introduction

Population increment, industrializing, and technologic development result directly in increasing energy consumption. This rapid growing trend brings approximately the very important environmental problems such as air pollution and greenhouse effect. Nowadays, about 80% of electricity in the world is produced from fossil fuel-fired thermal power plants [1–3].

Coal is the most abundant fossil energy resource in the world and exists in almost every major region of the world, but its quality varies greatly from region to region. Coal-fired thermal power plants (TPPs) are the most widely used plants worldwide. Actual electricity production of coal-fired TPPs is 41% of annual world electricity generation, and by 2030 this percentage is expected to rise to 44%. However, many countries use aged pulverized coal-fired boilers (PCBs) (25–40 years) for electricity generation. Moreover, coal (especially poor quality) used in these TPPs for electricity generation causes crucial environmental problems, such as global warming and acid rain, because the poor quality coal cannot be burned cleanly and efficiently in these boilers and their performance deteriorates. Hence, the thermal efficiency of TPPs is to be lower [1, 4–13].

Although the share of TPPs generating electricity is about 64% within the total installed power in Turkey; its ratio at the compensation of electricity demand is about 75% in 2012. Nowadays, more than 50% of the amount of electricity generated from TPPs is dependent on imported fuel sources, especially natural gas. It is obvious that the main solution of problems like these is efficient utilization of the domestic fuel sources. Therefore, enhancing the performance of the aged coal-fired TPPs is a necessity in terms of energy policy, national security, fuel reserve, and environmental concerns [1, 2, 14–16].

In the present work, firstly, economic analysis of rebuilding an aged pulverized coal-fired boiler (PCB) with a new pulverized coal-fired boiler including flue gas desulfurization

system (FGD) and a circulating fluidized bed boiler (FBB) are examined in an existing old thermal power plant. Secondly, emission costs are added to model, and the developed model is applied to a 200 MWe pulverized coal-fired thermal power plant in Turkey. Thirdly, the payback period and the net present value are calculated for different technical and economic parameters such as power loss, load factor, electricity price, discount rate, and escalation rate by using the annual value method. As a result, the outcomes of this study show that rebuilding of aged pulverized coal-fired boiler is a necessity for aging thermal power plants.

2. The Importance of Rebuilding

Because of the aging thermal power plants (TPPs) and so their equipment, thermal power plants also produce less power than their installed capacities, and there has been power loss in time. For example, boiler is one of the most important equipment in TPPs. Due to the aging of boilers, the problems such as slag and degradation of heat transfer increase and boilers produce less steam than their design values. As a result, TPPs also produce less power than their design values. Developing countries need more power and must build new plants to meet increasing demand. So, countries must recover power loss in aging TPPs, instead of making new investments. Moreover, chronic power shortages and scarcity of capital funds have led many countries to apply them to rebuilding of aging thermal power plants, instead of building new ones, because new power projects go through long environmental assessments and approval processes. Development of infrastructure for these projects, following the approval, also takes considerable time and entails high capital costs, whereas rebuilding of aging TPPs can be done in a relatively short time at a much lower cost. Therefore, TPPs can add more power to grid and benefit from recovering capacity through upgrades of old equipment such as aging boiler. In this connection, upgrading of aged pulverized coal-fired boilers (PCBs) can be one of the urgent needs for many countries because of the economic and environmental pressures [1, 6, 9, 14, 15].

In addition, aged PCBs must deal with both the decreasing quality of fuel and strict environmental standards. Moreover, the performance of these boilers is very bad, and emissions are very high. It is a vital issue to meet the increasing electricity demand and decrease emissions for many countries. Therefore, the rebuilding of aged PCBs with new one can be very important for adding more power to the grid and decreasing emissions.

3. Methodology

In this study, all costs and benefits during the economic lifespan of the system are expressed annually. Then, the payback period and the net present value are calculated for rebuilding of aged pulverized coal boiler (PCB) with a new PCB including flue gas desulfurization (FGD) unit and circulating fluidized bed boiler (FBB).

The rebuilding of aged PCB with a new PCB including flue gas desulfurization unit or a circulating FBB requires some changes, such as need for more area for FGD unit or replacement of super heaters. In addition, operation and maintenance costs will be different by rebuilding. Also, the thermal power plant is not operated throughout the rebuilding. Therefore, electricity is not sold during the rebuilding. Moreover, the results will change by adding FGD unit, because emissions will decrease. So, emission taxes will decrease. All these factors have been considered in the study. Because the proportion of auxiliary power consumption within total expenditure is very low, it is not taken into consideration in the analysis. Moreover, a similar methodology has been used, and assumptions have been taken as the same for two different technologies except for specific costs. Accordingly, total expenditure (E) and gain (G) can be calculated from (1) and (2), respectively [17–23].

Consider the following:

$$E = \left(C_I + C_D + C_O\right) N + R_L \ [\$], \tag{1}$$

$$G = G_E + G_F + G_{\mathrm{EM}} \ [\$/\mathrm{year}], \tag{2}$$

$$R_L = N_o \cdot \mathrm{LF} \cdot \mathrm{DP} \cdot P_e \ [\$], \tag{3}$$

$$G_E = H \cdot \mathrm{LF} \cdot \left(N - N_o\right) \cdot P_e \ [\$/\mathrm{year}], \tag{4}$$

$$G_{\mathrm{EM}} = G_{\mathrm{CO_2}} + G_{\mathrm{SO_2}} + G_{\mathrm{NO}_x} \ [\$/\mathrm{year}], \tag{5}$$

$$G_F = \frac{860 \cdot H \cdot N_o \cdot \mathrm{LF} \cdot P_f}{\mathrm{LHV}} \cdot \left(\frac{1}{\eta_{\mathrm{tho}}} - \frac{1}{\eta_{\mathrm{th}}}\right) \ [\$/\mathrm{year}], \tag{6}$$

where E is the total cost, C_I (\$/kWe) is the specific investment cost for new PCB with FGD, FBB, and auxiliary equipment, C_D (\$/kWe) is the specific cost of dismantling, erection, and commissioning, C_O (\$/kWe) is the specific constant operation and maintenance cost such as employees' salary, R_L is the revenue lost for the downtime period, G is the annual total gain, G_E is the annual additional electricity gain obtained from incremental power production, G_F is the annual additional gain because of fuel savings, G_{EM} is the annual gain due to the decrease in emissions after rebuilding, DP (h) is the downtime period, P_e (\$/kWeh) is the unit electricity price, P_f (\$/kg) is the unit fuel price, LHV (kcal/kg) is the low heat value of fuel, H (h) is the annual average operation duration of the plant, η_{tho} is the thermal efficiency of TPP before rebuilding, ηth is the thermal efficiency of TPP after rebuilding, N (kWe) is the installed power of the plant, N_o (kWe) is the operating power before revamping, and LF (%) is the annual average load factor of plant.

Unit emission cost is taken as \$0,22/kgCO_2, \$11/kgSO_2, and \$5,7/kgNO_x for CO_2, SO_2, and NO_x, respectively [17, 19, 20, 22, 23]. Then, annual emission costs are found and added to total gain.

Total expenditure (E) can be converted to annual constant expenditure (E_y) by using amortization factor (AF). Then, payback period (PBP) can be calculated (9). The payback period is the time of equality of the cost and benefit. Therefore, it is calculated with the rate of total annual constant expenditure (E_y) to total annual gain (G). Net present value (NPV) which includes escalation rates for electricity price and fuel price and discount rate can be determined from (10).

Table 1: Technical and economic parameters for the case study.

Description	Symbol	Unit	Value
Specific investment cost for FBB and auxiliary equipment	C_I	\$/kWe	220
Specific investment cost for new PCB with FGD and auxiliary equipment	C_I	\$/kWe	200
Specific investment cost for dismantling, erection, and commissioning for FBB rebuilding	C_D	\$/kWe	40
Specific investment cost for dismantling, erection, and commissioning for PCB with FGD rebuilding	C_D	\$/kWe	10
Specific operation and maintenance cost for FBB	C_O	\$/kWe	15
Specific operation and maintenance cost for new PCB with FGD	C_O	\$/kWe	5
Installed power of the plant	N	kWe	200
Existing operating power	N_o	kWe	160
Downtime period	DP	h	720
Load factor	L_f	%	85
Low heat value of fuel (1800 kcal/kg)	LHV	kJ/kg	7535
Thermal efficiency of TPP before revamping	η_{tho}	%	33
Thermal efficiency of TPP after revamping	η_{th}	%	35
Unit electricity price without fuel cost	P_e	\$/kWeh	0.035
Unit fuel price	P_f	\$/kg	0.04
Discount rate	r	%	5
Economic lifespan	n	Year	25

Consider the following:

$$E_y = E \cdot \text{AF} \ \left[\$/\text{year}\right], \tag{7}$$

$$\text{AF} = \frac{(1+r)^n \cdot r}{(1+r)^n - r}, \tag{8}$$

$$\text{PBP} = \frac{E_y}{G} \ \left[\text{year}\right], \tag{9}$$

$$\text{NPV} = \sum_{t=o}^{n} \left[B_{(t)} - C_{(t)}\right] \cdot (1+r)^{-t} \left[\$\right], \tag{10}$$

where n (year) is the economic life span, t is the period, and r (%) is the discount rate.

4. Case Study and Discussion

The prior aim of this study is to present a general economic model to evaluate quickly the rebuilding of aged pulverized coal-fired boiler (PCB) with a new one in existing thermal power plants (TPPs). Hence, it can be an important study for the evaluation of aging TPPs for researchers and operators of TPPs. Specific costs such as C_I, C_D, and C_O and technical data for case study have been taken from the literature ([1, 6, 15, 21]), authorities of Turkish Electricity Generation Co., Inc. (EUAS; http://www.euas.gov.tr/), and operators of Soma Thermal Power Plant (an institution of EUAS) in Manisa in Turkey. EUAS produces about half of Turkish electricity production, and it is a very important official institution of Turkey. Therefore, they are approximate values for case study. Conclusions of case study depend on these values. Moreover, auxiliary power consumption and boiler efficiency for two firing system are important parameters. Because the proportion of auxiliary power consumption within total expenditures is low and boiler efficiency for two firing system is very close to each other [6, 12], they are not taken into consideration in the analysis, but more accurate and sensitive solutions can be obtained from the development model by considering real cost values, auxiliary power consumption, and combustion efficiency.

Coal (especially lignite) is an important fuel source for Turkey and it is used mostly for electricity generation. On the basis of the latest estimates, the total lignite reserves of Turkey have reached approximately 11.5 billion ton. However, poor quality lignite (below 2000 kcal/kg) accounts for about 70% of these reserves. Share of better quality lignite (over 3000 kcal/kg) is very low (6%). The other lignite reserve (between 2001 and 3000 kcal/kg) accounts for about 24% [7, 16]. The developed model is applied to a 200 MWe pulverized coal-fired TPP in Turkey. Then, the payback period (PBP) and net present value (NPV) are computed. Coal quality effects PBP and NPV. Coal quality is directly related to lower heating value. The coal used in a 200 MWe thermal power plant example is poor quality coal (lower heating value is 1800 kcal/kg). Therefore, PBP decreases and NPV rises if the coal quality increases. Table 1 taken from the literature shows the technical and economic values for the case study [1, 6, 15, 16].

PBP and net present value NPV can change from country to country. Therefore, the effects of almost all technical and economic parameters, such as power loss, downtime period, escalation rate, and discount rate on PBP and NPV are investigated. As a result, it is seen that power loss has a significant effect on the NPV and PBP. When the power loss increases in the aged pulverized coal-fired TPP, the PBP decreases, and the NPV rises. So, the rebuilding is indispensable if power loss is high in aged pulverized coal-fired TPPs, especially after 30 MWe. NPV and PBP values are closer to each other for FBB and new PCB with FGD system when emission costs are not included (Figures 1 and 2), because TPPs can add more

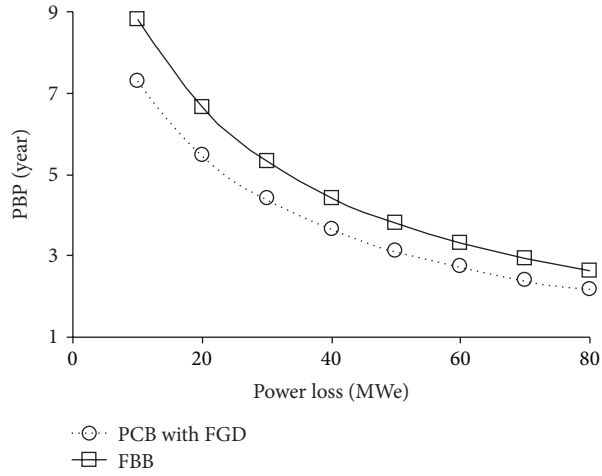

Figure 1: The variation of payback period (PBP) with power loss at PCB with FGD and FBB without emission costs.

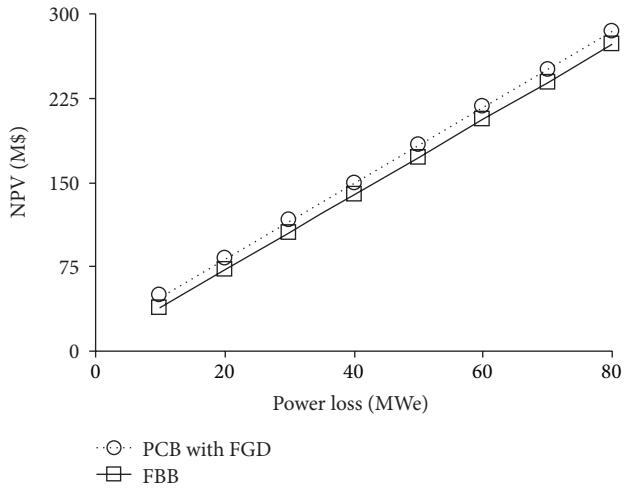

Figure 2: The variation of net present value (NPV) with power loss at PCB with FGD and FBB without emission costs.

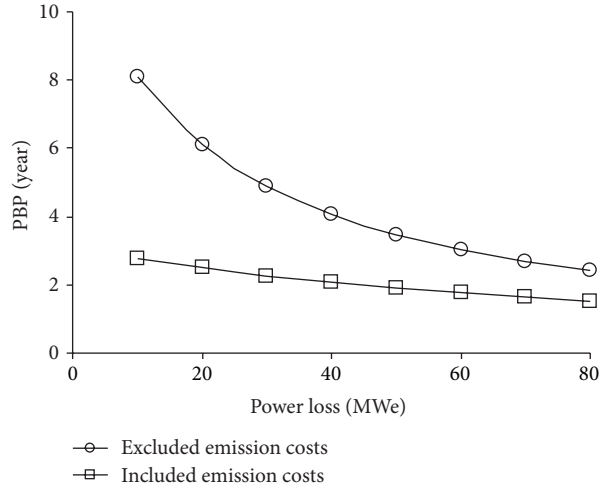

Figure 3: The variation of payback period (PBP) with power loss at FBB.

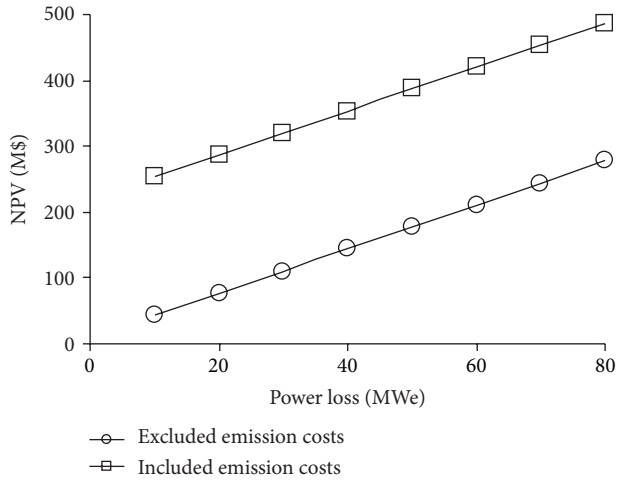

Figure 4: The variation of net present value (NPV) with power loss at FBB.

power to grid and benefit from recovering capacity through upgrades of aging equipment. The other parameters are also investigated in this study. However, their effects are less than power loss effects, so there is no place in this paper.

When the emission costs are added to FBB system, rebuilding is more advantageous (Figures 3 and 4). The results show the necessity of rebuilding with FBB in many countries when the taxes for emissions are engaged in the future. Besides, the results with emission taxes present the necessity of adding an eliminating system, because the PBP is decreasing and the NPV is increasing too much when the emission costs are eliminated. The difference between results includes and excludes emission taxes which are clearly seen from Figures 3 and 4.

Figures 5 and 6 show the variation of the payback period with downtime period and load factor at new PCB with FGD without emission costs, respectively. When the downtime period is decreased and the load factor is increased, payback period is diminished, because after rebuilding, income increases.

5. Conclusions and Suggestions

This study firstly presents a general economic model for the rebuilding of a pulverized coal boiler (PCB) with a new PCB including flue gas desulfurization (FGD) unit and circulating fluidized bed boiler (FBB). Secondly, a case study is performed for a 200 MWe aging pulverized coal-fired thermal power plant (TPP). Finally, the emission taxes are added to the model, and analysis is repeated.

Payback period (PBP) and net present value (NPV) are closer to each other for FBB and new PCB including FGD when emission costs are not included. Of the investigated parameters, power loss has the greatest effect on PBP and NPV. Therefore, if power loss is very high in the existing

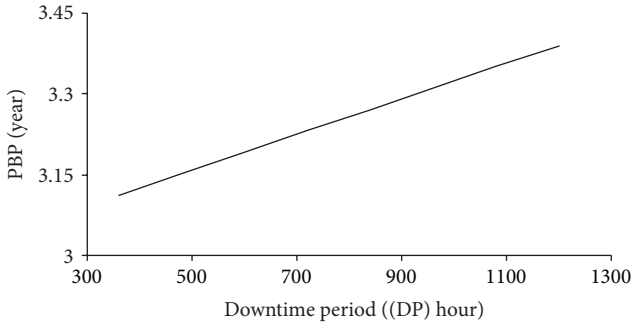

Figure 5: The variation of payback period with downtime period at new PCB with FGD without emission costs.

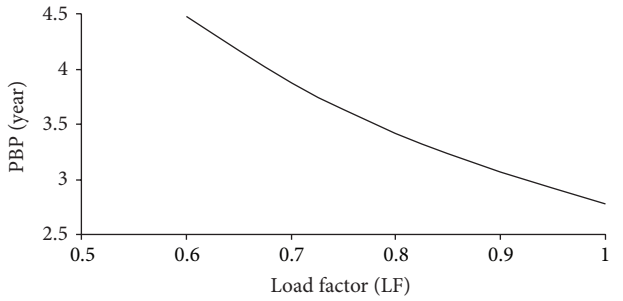

Figure 6: The variation of payback period with load factor at new PCB with FGD without emission costs.

TPP, the rebuilding will be very convenient. The more the increase of power loss at the old thermal power plant is, the more advantageous the rebuilding gets, especially after 30 MWe. The results show that the rebuilding of PCB with a new PCB with FGD unit system or FBB system is a cost-effective method, since it is amortized in a very short time.

Moreover, the results show the necessity of rebuilding when the taxes for emissions are engaged in a lot of countries in the future. When the emission costs are added to the model, rebuilding is more advantageous. When the emission taxes are added to the costs, the results are changing very much, the PBP is decreasing and the NPV is increasing too.

The prior aim of this study is to present a general economic model to evaluate quickly rebuilding of aged PCB with a new one in TPPs and to show that rebuilding of a PCB with a new one is a necessity. Technical and economic data in the case study are approximate values. Conclusions of the case study depend on these values. Therefore, more accurate and sensitive solutions can be obtained from the development model by considering real cost values, auxiliary power consumption, and combustion efficiency.

References

[1] B. Cetin, "Economic model for the revamping of a pulverized coal-fired boiler," *Energy Sources B*. In press.

[2] H. H. Erdem, A. V. Akkaya, B. Cetin et al., "Comparative energetic and exergetic performance analyses for coal-fired thermal power plants in Turkey," *International Journal of Thermal Sciences*, vol. 48, no. 11, pp. 2179–2186, 2009.

[3] Ü. Çamdali and V. Ş. Ediger, "Optimization of fossil fuel sources: an exergy approach," *Energy Sources A*, vol. 29, no. 3, pp. 251–259, 2007.

[4] H. H. Erdem, A. Dagdas, S. H. Sevilgen et al., "Thermodynamic analysis of an existing coal-fired power plant for district heating/cooling application," *Applied Thermal Engineering*, vol. 30, no. 2-3, pp. 181–187, 2010.

[5] B. G. Miller and S. F. Miller, "Fluidized-bed firing systems," in *Combustion Engineering Issues For Solid Fuel Systems*, B. G. Miller and D. A. Tillman, Eds., chapter 8, Elsevier, 2008.

[6] S. Kavidass, D. J. Walker, and G. S. Norton, "IR-CFB Repowering: a cost-effective option for older pc-fired boilers," in *POWER-GEN International '99*, New Orleans, Lo, USA, December 1999.

[7] A. Hepbasli, "Coal as an energy source in Turkey," *Energy Sources*, vol. 26, no. 1, pp. 55–63, 2004.

[8] N. Eskin and A. Hepbasli, "Development and applications of clean coal fluidized bed technology," *Energy Sources A*, vol. 28, no. 12, pp. 1085–1097, 2006.

[9] P. Basu and P. K. Halder, "New concept for operation of a pulverized coal-fired boiler using circulating fluidized bed firing," *Journal of Engineering for Gas Turbines and Power*, vol. 111, no. 4, pp. 626–630, 1989.

[10] P. Basu, "Combustion of coal in circulating fluidized-bed boilers: a review," *Chemical Engineering Science*, vol. 54, no. 22, pp. 5547–5557, 1999.

[11] G. A. Ryabov, O. M. Folomeev, D. S. Litun, D. A. Sankin, and I. G. Dmitryukova, "Prospects for using the technology of circulating fluidized bed for technically refitting Russian thermal power stations," *Thermal Engineering*, vol. 56, no. 1, pp. 31–40, 2009.

[12] S. Kavidass, G. L. Anderson, and G. S. Norton, "Why build a circulating fluidized bed boiler to generate steam and electric power," in *POWER-GEN Asia '00*, Bangkok, Thailand, September 2000.

[13] J. Koornneef, M. Junginger, and A. Faaij, "Development of fluidized bed combustion-An overview of trends, performance and cost," *Progress in Energy and Combustion Science*, vol. 33, no. 1, pp. 19–55, 2007.

[14] P. Basu, "Operation of an existing Pulverized-Coal fired boiler as a circulating fluidized bed boiler—a conceptual study," *Journal of the Institute of Energy*, vol. 60, no. 443, pp. 77–83, 1987.

[15] M. Abacioglu, *Investigation of a pulverized coal boiler with circulating fluidized bed boiler in an existing thermal power plant [M.S. thesis]*, Yildiz Technical University Graduate School of Natural and Applied Science, Istanbul, Turkey, 2012.

[16] http://www.euas.gov.tr/Sayfalar/YillikRaporlar.aspx.

[17] Å. Karlsson and L. Gustavsson, "External costs and taxes in heat supply systems," *Energy Policy*, vol. 31, no. 14, pp. 1541–1560, 2003.

[18] T. Berntsson, *Heat Sources-Technology, Economy and Environment*, Department of Heat & Power Technology. Chalmers University of Technology, Göteborg, Sweden, 1999.

[19] J. Sjödin, "Modelling the impact of energy taxation," *International Journal of Energy Research*, vol. 26, no. 6, pp. 475–494, 2002.

[20] T. Hamacher, R. M. Sáez, K. Aquilonius et al., "A comprehensive evaluation of the environmental external costs of a fusion power plant," *Fusion Engineering and Design*, vol. 56-57, pp. 95–103, 2001.

[21] B. Sahin and N. Aybers, *Energy Cost*, Yildiz Technical University Press, Istanbul, Turkey, 1995.

[22] E. Fahlén and E. O. Ahlgren, "Accounting for external costs in a study of a Swedish district-heating system—an assessment of environmental policies," *Energy Policy*, vol. 38, no. 9, pp. 4909–4920, 2010.

[23] T. Kosugi, K. Tokimatsu, A. Kurosawa, N. Itsubo, H. Yagita, and M. Sakagami, "Internalization of the external costs of global environmental damage in an integrated assessment model," *Energy Policy*, vol. 37, no. 7, pp. 2664–2678, 2009.

Hindawi Publishing Corporation
Advances in Mechanical Engineering
Volume 2013, Article ID 474935, 8 pages
http://dx.doi.org/10.1155/2013/474935

Research Article

Simulation and Experimental Investigation of Thermal Performance of a Miniature Flat Plate Heat Pipe

R. Boukhanouf[1] and A. Haddad[2]

[1] *Department of the Built Environment, University of Nottingham, Nottingham NG7 2RD, UK*
[2] *FrigoDynamics GmbH, Bahnhofstraße 16, 85570 Markt Schwaben, Germany*

Correspondence should be addressed to R. Boukhanouf; rabah.boukhanouf@nottingham.ac.uk

Received 4 February 2013; Accepted 25 March 2013

Academic Editor: Godson Asirvatham Lazarus

This paper presents the results of a CFD analysis and experimental tests of two identical miniature flat plate heat pipes (FPHP) using sintered and screen mesh wicks and a comparative analysis and measurement of two solid copper base plates 1 mm and 3 mm thick. It was shown that the design of the miniature FPHP with sintered wick would achieve the specific temperature gradients threshold for heat dissipation rates of up to 80 W. The experimental results also revealed that for localised heat sources of up to 40 W, a solid copper base plate 3 mm thick would have comparable heat transfer performances to that of the sintered wick FPHP. In addition, a marginal effect on the thermal performance of the sintered wick FPHP was recorded when its orientation was held at 0°, 90°, and 180° and for heat dissipation rates ranging from 0 to 100 W.

1. Introduction

Conventional heat sink-fan air coolers in electronics packages are becoming inadequate for use in faster, compact, and more powerful multitasked microprocessors that generate large quantities of attendant heat. This has led current research to focus on high-performance and compact thermal solutions [1]. Heat pipes have been extensively researched and applied in various embodiments for electronics cooling ranging from simple cylindrical geometries to complex configurations [2]. FPHPs in particular have high-heat transfer capability, can maintain a uniform temperature over the evaporator surface when densely packed with heat-generating components, and decrease the thickness of finned heat sinks base material [3–6].

Recent research by Christensen and Graham [7] investigated the performance of heat sinks in packaging high-power (>1 W) light-emitting diode (LED) arrays and concluded that flat plate heat pipes form an important thermal component to achieve long operating life and high reliability. Huang and Liu [8] demonstrated analytically the increased capability of mounting a localised heat source and heat sink on the same surface of an FPHP. Similarly, Qin and Liu [9] investigated liquid flow in an anisotropic permeability wick of a flat plate heat pipe, determining the effect of heat source location on fluid distribution in the inside of the heat pipe. Further work on finding the optimum location of mounting multiple heat sources on an FPHP evaporator surface was demonstrated by Tan et al. [10] through a simplified analytical solution to a two-dimensional pressure and velocity distribution within the wick. Recently, Sonan et al. [11] developed a simulation model for the transient thermal performance of a 40 × 40 × 0.9 mm FPHP with specific applications to cooling multiple electronics components where space restriction imposes that heat sources and heat sinks need to be mounted on the same surface. The above research agrees that a cost premium associated with a well-designed FPHP for advanced thermal management solution in electronics cooling should be reflected in its superior thermal performance compared to solid copper or aluminium base materials of similar dimensions.

This paper investigates the design and thermal performance of a miniature FPHP as an effective supporting shelf for printed circuit boards (PCB) of radio frequency (RF)

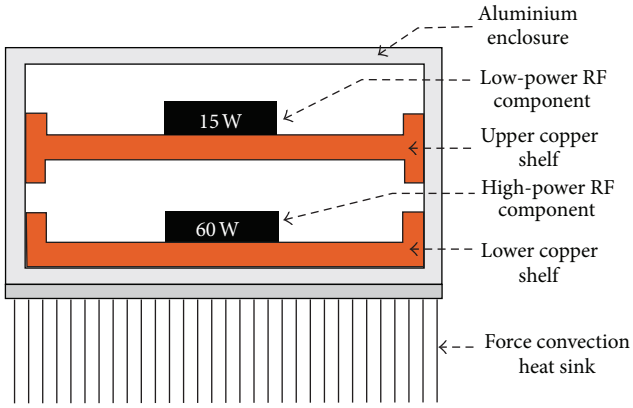

Figure 1: Schematic of the electronics cooling enclosure.

components to dissipate and transport heat away to the aluminium enclosure. In this paper, two identical miniature FPHPs configurations one with a sintered copper powder and the other one with a screen copper mesh wick were designed and tested. A further benchmarking exercise, using both CFD analysis and experimental measurements, was carried out by comparing the thermal performance of the FPHP to that of a monolithic solid copper plate with similar dimensions.

2. Description of the Electronics Enclosure Cooling System

The work addresses the cooling requirement to maintain a specified temperature limit for heat-generating RF components that are housed in an existing aluminium enclosure as part of a large telecommunication control system. The aluminium enclosure consists of two separate copper shelves and an air cooled finned base plate, as shown in Figure 1. The PCB of high heat dissipating RF components was mounted on the lower shelf of the enclosure to allow for direct contact with the base heat metal spreader while low-power rated RF components were placed on the top shelf. In the original design, the enclosure's shelves were made of 1 mm thick copper base. However, frequent and premature failures of RF components prompted the review of the enclosure's thermal performance. Hence, a redesign of the copper shelves to keep the operating temperature gradients of the RF components within the specified limits was performed using both CFD simulation and an experimental validation analysis. The work consists in investigating the thermal performance of the enclosure's shelves that are made of a 1 mm and 3 mm solid copper base plates and two miniature FPHPs of 5 mm overall height with one using sintered copper powder wick and the other one a screen mesh wick.

2.1. FPHP Design. The FPHP base material was made of copper material and water was selected as the working fluid for its compatibility and suitable operating temperature range. The outer shell of the constructed prototype miniature FPHPs for the sintered and mesh wicks is shown in Figure 2(a). The inner structure of the sintered wick FPHP with the condenser cover plate removed to reveal the sintered wick layer and erected pillars on the evaporator surface is shown in Figure 2(b). Similarly, the structure of the miniature FPHP with copper mesh wick is shown in Figure 2(c). The design of the mesh wick FPHP was adopted from Bakke [12] and Rosenfeld et al. [13], which consists of using a fine mesh layer to provide capillary pumping force of the working fluid and a coarse mesh to support and maintain the structural integrity of the vapour space.

2.2. FPHP CFD Simulation. The thermal performance of the miniature FPHP was simulated using FloTHERM, a commercial CFD simulation software. The computer simulation includes analysing the complex flow pattern of the working fluid in the wick and establishing the temperature profiles in the FPHP evaporator. Flotherm is a finite volume-based software package that uses simple Cartesian grid meshing and has built in boundary conditions for common heat transfer devices. The rectangular shape of the FPHP, heater block, and cold plate lend themselves well to meshing using Cartesian coordinates and hence the use of Flotherm for a fast and converging solution. Description of the mathematical model for momentum, mass, and energy conservation that underpin the CFD simulation was not the focus of this paper as similar models are widely available in published literature that can be found in [14–16].

The Flotherm model was built using standard Cuboids and Prism elements for the FPHP components including the evaporator and condenser copper plates, the wick layer, the void (vapour) space, and the supporting solid columns. Planar resistance object model was used to define the thermal properties for each object. This is a useful tool where the thermal resistance of an object can be inserted manually or determined from other thermal parameters such as the thermal conductivity and heat transfer coefficient. Modelling of the porous wick layer, in particular, requires prior knowledge of the permeability of the porous wick structure. The volumetric flow rate, $\dot{V}$, of the working fluid was also required as an input parameter in the simulation. This was calculated from the following relationship:

$$\dot{V} = \frac{\dot{Q}_H}{\rho_l h}, \tag{1}$$

where $\dot{Q}_H$ is the rate of heat generation in the heat source and h, and ρ_l are the latent heat and density of the working fluid, respectively. In addition, it is well known that the failure of heat pipes is often attributed to operation beyond the device's wick capillary limit. This can be obtained by characterising the actual pressure of the liquid in the wick pores under different heat flux levels using Laplace-Young equation as follows [1]:

$$\Delta p_c = \frac{2\sigma_l}{r_{\text{pore}}}, \tag{2}$$

where Δp_c is the capillary pressure drop in the wick, σ_l is the surface tension of the liquid, and r_{pore} is the pore radius of the wick.

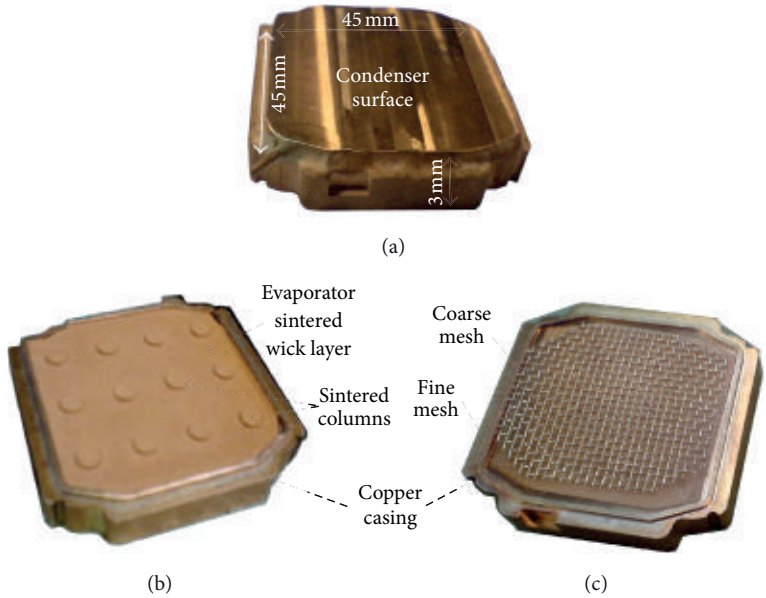

Figure 2: Constructed miniature FPHP (a) sealed unit, (b) sintered wick, and (c) mesh wick.

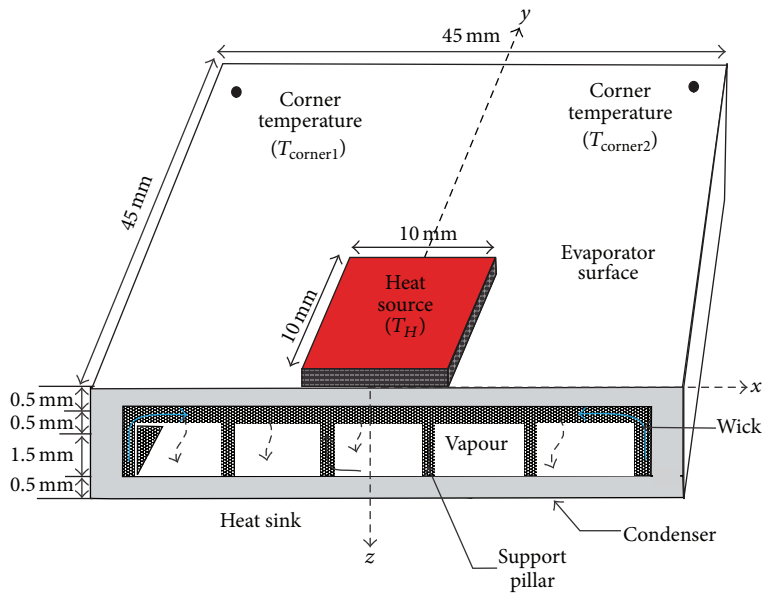

Figure 3: A schematic representation of the FPHP.

Equally, the effective thermal conductivity of a saturated wick, k_{eff}, was obtained from the following expression [17, 18]:

$$k_{\text{eff}} = \beta\left(\varphi k_l + (1-\varphi)\, k_s\right) + \frac{(1-\beta)}{\varphi/k_l + (1-\varphi)/k_s}, \quad (3)$$

where φ is the porosity of the wick, k_l and k_s are the thermal conductivity of liquid water and solid wick, respectively. According to Bhattacharya et al. [17], the best-fit data for measuring the effective thermal conductivity of a porous material is for $\beta = 0.35$ with an overall R^2 value of 0.97. This is consistent with measured thermal conductivities of about 40 W/(mK) in heat pipes with fully saturated wicks, while the vapour space is considered to have a very large heat transfer coefficient of the order of 50000 W/m^{2}K [16, 18].

A schematic representation of the sintered wick heat pipe given in Figure 3 illustrates the location of the heat source, a cross section of the wick layer, the working fluid circulation paths, and the condenser cold plate heat sink.

In this analysis, it was also assumed that the heat source is of constant heat flux type which is applied to the evaporator base plate (at $z = 0$) immediately under the heat source while

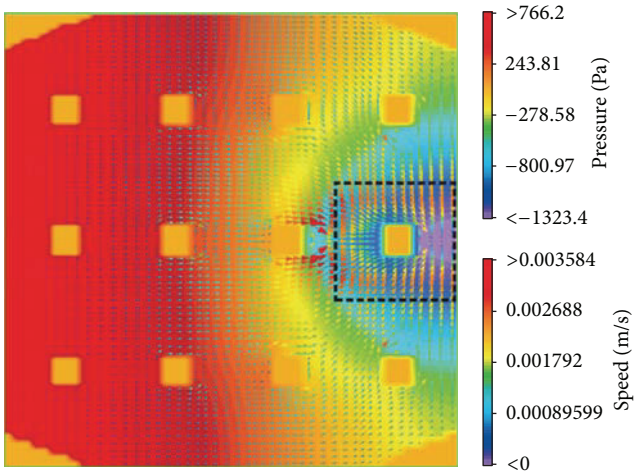

Figure 4: CFD simulation of speed and pressure fields of the liquid in the FPHP-sintered wick (Q_H = 80 W).

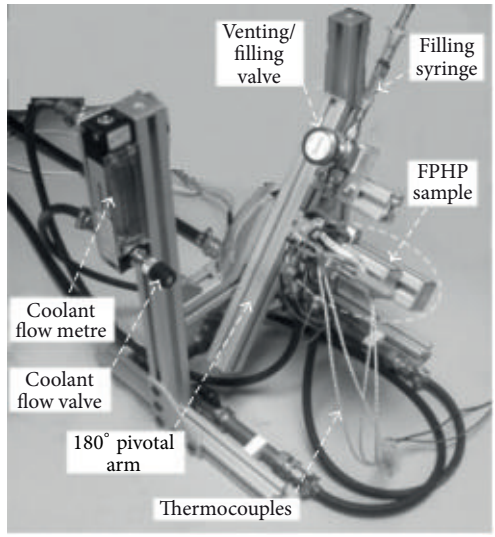

Figure 5: The experimental test rig setup.

the remaining outer surface of the evaporator including the edge walls is considered to be adiabatic. In the inner section of the heat pipe, it was assumed that the liquid-vapour interface temperature is equal to the vapour saturation temperature of the working fluid that can be calculated from Clausius-Clapeyron relationship [19]. Similarly, the liquid velocity at the interface of the wick layer-evaporator wall was assumed to equal zero. At the condenser-vapour interface, the temperature of the condenser section was maintained at 35°C using a chilled liquid cold plate with a heat transfer coefficient in the order of 2000 W/(m^{2}K).

A thermocouple placed at the interface surface between the evaporator and heat source was used to measure the temperature of the heater block, T_H, and a further two thermocouples were placed at the two farthest corners on the evaporator to measure T_{corner1} and T_{corner2}. Furthermore, the heat dissipation from the RF components was simulated

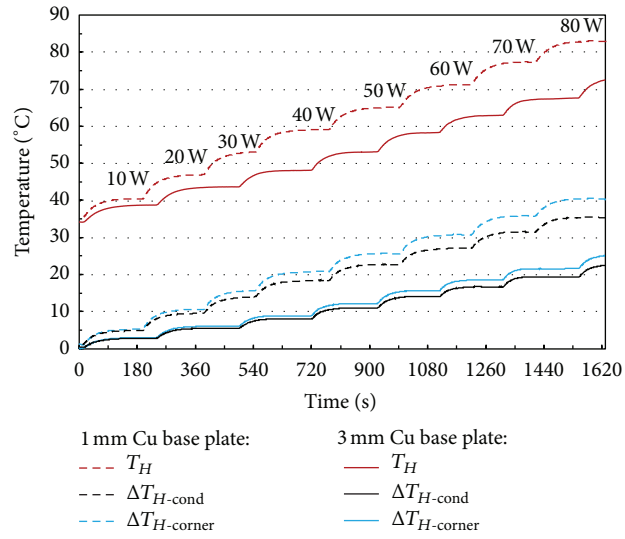

Figure 6: Temperature variation of a 1 mm and 3 mm thick copper base plates.

Table 1: Design properties of the sintered and mesh wick miniature FPHP.

Casing	
Material	Copper
Height	3 mm
Dimension	45 mm × 45 mm
Heater block size	10 mm × 10 mm
Working fluid	Water
Sintered copper powder wick	
Wick thickness	0.5 mm
Vapour space height	1.5 mm
Porosity	50%
Pore radius	40 μm
Permeability	1.43×10^{-11} m^2
Screen copper mesh wick	
Fine mesh material	Phosphor bronze 320 mesh/in
Wire diameter	0.03 mm
Porosity	42%
Wick thickness	1 mm
Supporting coarse mesh material	Phosphor bronze 16 mesh/in

using an electric heater cartridge that is inserted in a solid aluminium block of 10 mm × 10 mm with a controlled heat dissipation rates. The condenser surface was maintained to the desired temperature of 35°C by clamping directly onto its surface a chilled water cold plate. The main design properties of the miniature FPHPs with sintered and mesh wicks are given in Table 1.

2.3. CFD Simulation Results. The CFD simulation was used to evaluate the sintered wick FPHP thermal performance by

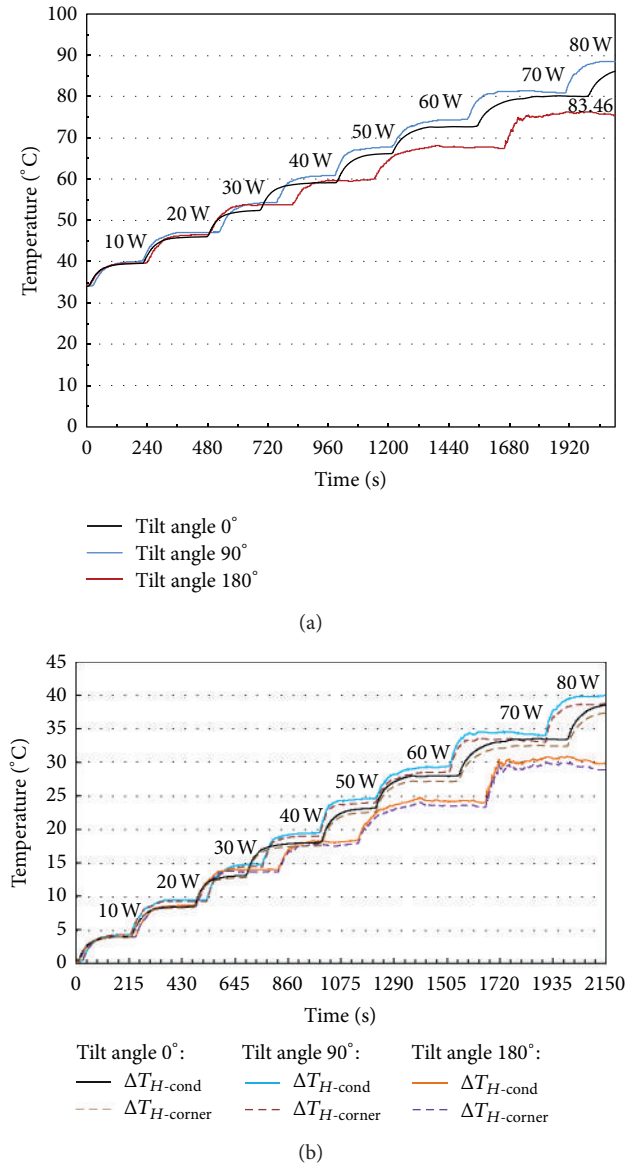

Figure 7: Screen mesh wick FPHP temperature variation at various heat dissipation levels and tilt angles: (a) heat source temperature, (b) evaporator surface temperature gradient.

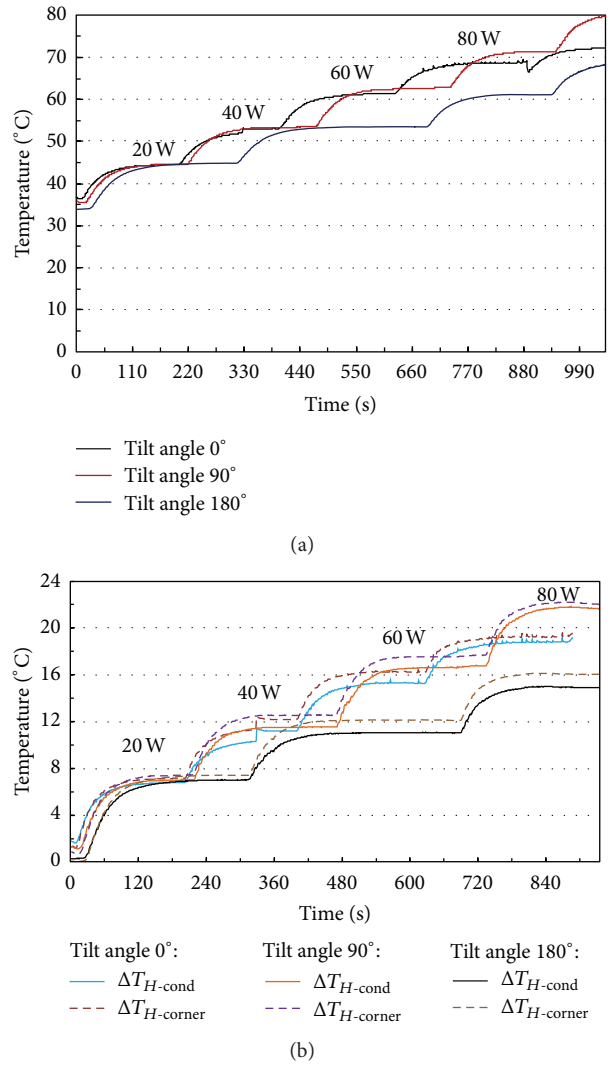

Figure 8: Sintered wick FPHP temperature at various heat dissipation levels and tilt angles: (a) heat source temperature, (b) surface temperature gradient.

analysing the steady state liquid flow pressure and velocity distribution in the sintered wick as shown in Figure 4. The speed of the liquid flow in the wick structure is presented by arrows pointing towards the heat source (dashed line square) and arranged by colour in contours of equal speeds. It can be seen that the speed of the liquid flow is lowest at regions most distant from the heat source (contours of purple arrows) and increases gradually as the liquid is drawn towards the heat source (contours of orange and red arrows) to replenish the evaporated liquid from the wick pores in the constant heat flux section. The liquid flow speed then drops sharply in the region immediately underneath the heat source as the liquid evaporates from the wick. The effect of the sintered pillars is also visible in that the liquid flow speed field contours are altered in a way that high-fluid speed spots were developed around the pillars. Furthermore, Figure 4 shows the liquid pressure distribution in the wick with the high pressure region (in red colour) away from the heat source and the low-pressure regions (in blue/purple colour) immediately beneath the heat source.

From the CFD analysis, it was found that the total pressure difference generated by the capillary forces of the wick is 2089.6 N/m^2. This is markedly lower than the capillarity pumping limit of the wick of 3952 N/m^2 which was calculated using (2) under the working conditions given in Table 2.

3. Experimental Setup and Results

The experimental rig setup to test the thermal performance of the miniature FPHP and solid copper base samples is shown in Figure 5. The rig was equipped with a liquid filling

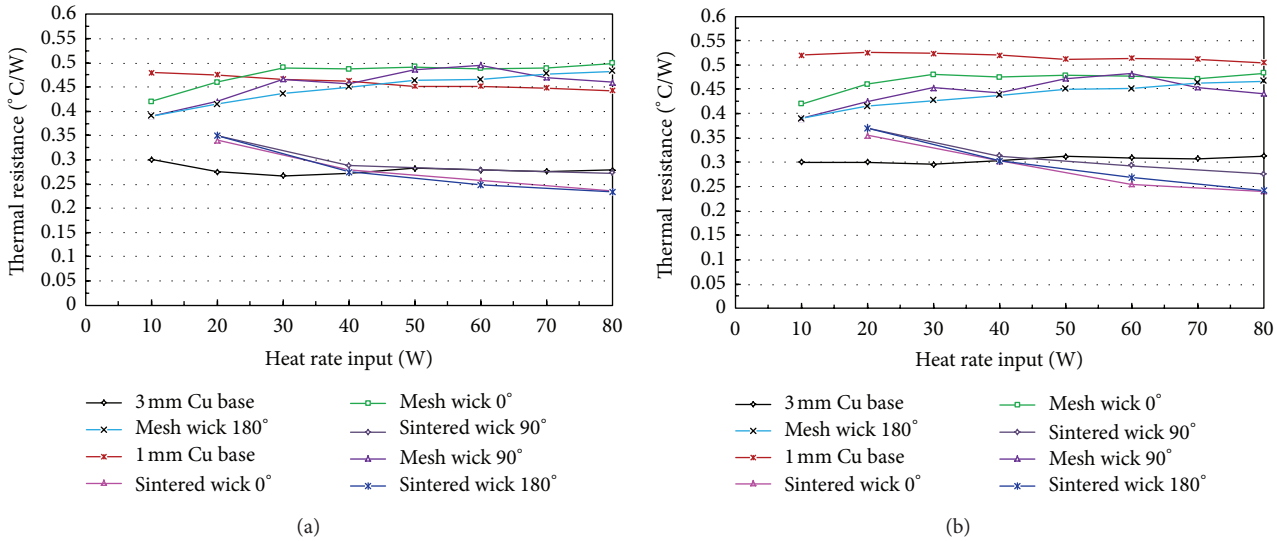

Figure 9: Thermal resistance: (a) one dimensional resistance, (b) spreading resistance.

Table 2: Saturated wick operating properties.

Heat load $\dot{Q}_H$ (W)	Liquid surface tension σ_l (kg/s^2)	Liquid density ρ_l (kg/m^3)	Liquid latent heat of vaporisation h (kJ/kg)	Sintered powder wick permeability $\varepsilon_{\text{wick}}$ (m^2)	Liquid flow rate from (1) $\dot{V}$ (m^3/s)	Pressure drop from (2) ΔP_c (N/m^2)	Pressure drop (CFD) ΔP_{CFD} (N/m^2)
80	0.0626	972	2310	$1.43E-11$	$3.563E-08$	3952	2089.6

Table 3: Sintered wick FPHP thermal resistance calculation uncertainty.

Heat input (W)	20	40	60	80
Calculated thermal resistance uncertainty (%)	13.60	6.00	4.14	3.80

and venting system for charging the FPHP, a rotating beam for mounting the heat pipe at different tilt angles (0° to 180°), a variable power supply to control heat dissipation from the heat source, a chilled water supply to control the condenser temperature, and associated sensors and data acquisition equipment. The miniature FPHP test sample was clamped onto the tilting beam with 0° angle being designated for operation against gravity (i.e., evaporator is above the condenser). An electric heater cartridge placed inside an aluminium block of 10 mm × 10 mm was used as heat source which heat dissipation rate was controlled by a variable power supply. A thermal interface material 0.5 mm thick was used as an interface between the FPHP test sample, the heater block, and the condenser cold plate to minimise the contact thermal resistances.

The performance of the FPHP test sample was evaluated at various heat dissipation rates by increasing the heat source power at equal increments of 10 W to a maximum of 100 W or until the temperature of the evaporator surface reached a threshold of 100°C. At each heat input increment the temperature of the evaporator surface was allowed to reach steady state. In addition, the effect of orientation on the FPHPs was evaluated by repeating the experimental measurements at tilt angles of 0°, 90°, and 180°. For comparison, further experimental tests were conducted on a 1 mm and 3 mm thick solid copper base plates under identical controlled conditions. In all tested samples, the operating temperature was measured at the heat source, T_H, evaporator plate corners T_{corner1} and T_{corner2}, and at the condenser surface, T_{cond}.

3.1. Solid Copper Base Plate Shelves. The initial tests of two solid copper plates of 45 mm × 45 mm and a thickness of 1 mm and 3 mm were carried out to provide a benchmark data which the thermal performance of the FPHPs was compared to. Results of these tests are shown in Figure 6, where it can be seen that for the same heat dissipation rates the temperature of the heat source in the 1 mm thick copper base is higher than that of the 3 mm thick copper base, particularly at high heat dissipation rates. For example, at a heat dissipation rate of 80 W, the recorded temperature, T_H, is 84°C and 73°C for the 1 mm and 3 mm thick base plates, respectively. Similarly, the temperature gradients between the heat source and the two far end corners, $\Delta T_{H\text{-corner}}$, and between the heat source and the heat sink, $\Delta T_{H\text{-cond}}$, are approximately 15°C higher for the 1 mm thick copper base than for its 3 mm thick counterpart. This shows that the 3 mm thick copper base plate has superior heat-spreading properties as predicated in the CFD simulation results.

3.2. Screen Mesh Wick Miniature FPHP. The procedure for evaluating the thermal performance of the screen mesh

wick FPHP was similar to that presented in previous case with additional experimental measurements to assess the effect of orientation at tilt angles of 0°, 90°, and 180°. The measured temperature changes at the heat source and across the evaporator surface are shown in Figures 7(a) and 7(b). These show that at 0° and 90° tilt angles the FPHP performance is only comparable to that of the 1 mm thick solid copper base. For example at high-heat dissipation rates (80 W), the temperature of the heat source approaches 90°C and a large temperature gradient (30 to 40°C) appears across the evaporator surface and between the heat source and heat sink, $\Delta T_{H\text{-cond}}$. The thermal performance of the heat pipe has improved marginally for a tilt angle of 180° (gravity assisted wick capillary forces), but it remains that the 3 mm solid copper base plate performed better. This unexpected poor thermal performance may be attributed to the process of fabrication in which poor contact between the fine screen mesh and the inner evaporator wall could have prevented liquid circulation, leading to a high interfacial thermal resistance.

3.3. Sintered Copper Powder Wick FPHP. The sintered wick FPHP thermal performance is shown in Figures 8(a) and 8(b). It can be seen that for a heat dissipation rate of 80 W the measured temperature of the heat source at a tilt angle of 0° is 69°C, which is lower by 15°C and 5°C compared to the 1 mm and 3 mm copper base plates, respectively. For a tilt angle of 180° the temperature of the heat source has dropped even further to 61°C, an improvement of 12°C compared to the 3 mm copper base plate. Similarly, the measured temperature gradients $\Delta T_{H\text{-cond}}$ and $\Delta T_{H\text{-corner}}$ are 6°C and 5°C lower than that of the 3 mm copper base plate for a tilt angle of 0° and 10°C and 8°C for a tilt angle of 180°, respectively.

The high-thermal performance of the sintered wick miniature is due to high heat conduction and spreading capability of the sintered wick compared to a simple monolithic solid copper base plate or screen mesh wick FPHP.

4. Evaluation of Bulk and Thermal Spreading Resistance

The effective thermal resistance of an electronics component mounted on a PCB is the sum of a one-dimensional bulk resistance and a thermal spreading resistance. The one-dimensional bulk thermal resistance is expressed as follows [4, 20, 21]:

$$R_b = \frac{T_H - T_{\text{cond}}}{\dot{Q}_H}. \tag{4}$$

The thermal spreading resistance is associated, however, with discrete heat-generating components when mounted on a cold base plate, as found in electronics packages. The thermal spreading resistance characterises the ability of a base plate to spread the heat uniformly across the base plate surface (or the evaporator surface in the case of FPHP). The thermal spreading resistance could be of a similar magnitude to the one-dimensional bulk resistance in some designs of heat exchangers. Hence, its omission can lead to significant errors in estimating the temperature of a PCB, resulting in components overheating and failing prematurely. The thermal spreading resistance, R_{sp}, is computed using the following expression [21]:

$$R_{\text{sp}} = \frac{T_H - \left(T_{\text{corner1}} + T_{\text{corner2}}\right)/2}{\dot{Q}_H}. \tag{5}$$

The variation of the one-dimensional bulk and thermal spreading resistances for the tested copper base plates and miniature FPHPs are shown in Figure 9. It can be seen that for heat dissipation rates of up to 40 W, the sintered wick heat pipe and the 3 mm thick copper base plate have comparable thermal performances in that both the one-dimensional and spreading thermal resistances are of similar magnitude. For higher heat dissipation rates, however, the advantage of a sintered wick FPHP becomes more apparent as the one-dimensional bulk and thermal spreading resistances are lower compared to other designs.

Finally, the uncertainty error of calculating the one-dimensional bulk and thermal spreading resistances is estimated from the measured data and the accuracy of the instruments used in the experiments. The accuracy of the T-type thermocouples is 0.5°C while the average error for power supply reading (wattmeter) is estimated at 2.3 W. Therefore, using the single sample analysis [22], the relative uncertainty error of the thermal resistance is calculated as follows:

$$e_R = \sqrt{\left(\frac{e_T}{\Delta T}\right)^2 + \left(\frac{e_Q}{\dot{Q}_H}\right)^2}. \tag{6}$$

It was assumed that the electrical power input to the heater block was fully dissipated as heat energy and that heat loss by convection and radiation from the test sample was negligible. The relative uncertainty error calculation of the thermal resistances has been limited to the case of the sintered wick FPHP, as shown in Table 3. The uncertainty calculation of the FPHP thermal resistance decreases from 13.6% to 3.8% for heat input rates of 20 W and 80 W, respectively. Although the average reading accuracy of the wattmeter is 2.3 W, the reading scale is nonlinear and the error of measurement is highest at low end of the scale, leading to large uncertainty of the measured thermal resistance for a heat rate input of 20 W.

5. Conclusion

This work investigated the thermal performance of a miniature FPHPs with sintered and screen mesh wicks for application in electronics cooling. The thermal performance of the FPHPs was further compared to that of copper solid base plates 1 mm and 3 mm thick. The ability of each sample to dissipate heat was evaluated by measuring the temperature distribution on the mounting surface and the temperature gradient between the heat source and heat sink. The main findings can be summarised as follows.

(i) The CFD results of predicting that the sintered wick FPHP would perform better than other arrangements were in good agreement with the experimental measurements.

(ii) It was found that the 3 mm thick copper base plate thermal performance surpasses that of the 1 mm and achieves higher heat conduction and spreading performance than the screen mesh wick FPHP.

(iii) The 3 mm thick copper base can perform adequately with heat dissipation rates of up to 40 W.

(iv) For heat dissipation rates higher than 40 W, the sintered wick FPHP outperforms the 3 mm copper base plate and its application would justify its high cost.

(v) The temperature measured on the evaporator surface of the sintered wick FPHP shows that there is no sign of liquid dry-out conditions in the wick for the range of heat dissipation rates.

(vi) The orientation of the sintered wick FPHP had marginal effect on its performance.

Acknowledgments

The authors wish to thank EPSRC (Engineering and Physical Sciences Research Council) for its financial support of the project under Grant EP/P500389/1 and Thermacore Europe Ltd for providing financial and technical help.

References

[1] D. A. Reay and P. A. Kew, *Heat Pipes: Theory, Design and Applications*, Butterworth-Heinemann, New York, NY, USA, 5th edition, 2006.

[2] M. Groll, "Heat pipe research and development in western Europe," *Heat Recovery Systems and CHP*, vol. 9, no. 1, pp. 19–66, 1989.

[3] A. Basiulis, H. Tanzer, and S. McCabe, "Thermal management of high power PWB's through the use of heat pipe substrates," in *Proceedings of the 6th Annual International Electronics Packaging Conference*, vol. 6, p. 501, San Diego, Calif, USA, 1986.

[4] M. Adami and B. Yimer, "Development and evaluation of a planar heat pipe for cooling electronic systems," *Chemical Engineering Communications*, vol. 90, no. 1, pp. 57–74, 1990.

[5] S. W. Kang, S. H. Tsai, and H. C. Chen, "Fabrication and test of radial grooved micro heat pipes," *Applied Thermal Engineering*, vol. 22, no. 14, pp. 1559–1568, 2002.

[6] C. Y. Liu, C. Y. Liu, K. C. Leong, Y. W. Wong, and F. L. Tan, "Performance study of flat plate heat pipe," in *Proceedings of the International Conference on Energy and Environment (ICEE)*, pp. 512–518, Begell House Inc., New York, NY, USA, 1996.

[7] A. Christensen and S. Graham, "Thermal effects in packaging high power light emitting diode arrays," *Applied Thermal Engineering*, vol. 29, no. 2-3, pp. 364–371, 2009.

[8] X. Y. Huang and C. Y. Liu, "The pressure and velocity fields in the wick structure of a localized heated flat plate heat pipe," *International Journal of Heat and Mass Transfer*, vol. 39, no. 6, pp. 1325–1330, 1996.

[9] W. Qin and C. Y. Liu, "Liquid flow in the anisotropic wick structure of a flat plate heat pipe under block-heating condition," *Applied Thermal Engineering*, vol. 17, no. 4, pp. 339–349, 1997.

[10] B. K. Tan, X. Y. Huang, T. N. Wong, and K. T. Ooi, "A study of multiple heat sources on a flat plate heat pipe using a point source approach," *International Journal of Heat and Mass Transfer*, vol. 43, no. 20, pp. 3755–3764, 2000.

[11] R. Sonan, S. Harmand, J. Pellé, D. Leger, and M. Fakès, "Transient thermal and hydrodynamic model of flat heat pipe for the cooling of electronics components," *International Journal of Heat and Mass Transfer*, vol. 51, no. 25-26, pp. 6006–6017, 2008.

[12] A. P. Bakke, "Light weight rigid flat plate heat pipe utilizing copper foil container laminated to heat treated Aluminium plates for structural stability," US Patent No. 6679318 B2, 2004.

[13] J. H. Rosenfeld, N. J. Gernert, D. V. Sarraf, P. Wollen, F. Surina, and J. Fale, "Flexible heat pipe," US Patent No. 6446706 B1, 2002.

[14] Y. Koito, H. Imura, M. Mochizuki, Y. Saito, and S. Torii, "Numerical analysis and experimental verification on thermal fluid phenomena in a vapor chamber," *Applied Thermal Engineering*, vol. 26, no. 14-15, pp. 1669–1676, 2006.

[15] G. Carbajal, C. B. Sobhan, G. P. Bud Peterson, D. T. Queheillalt, and H. N. G. Wadley, "A quasi-3D analysis of the thermal performance of a flat heat pipe," *International Journal of Heat and Mass Transfer*, vol. 50, no. 21-22, pp. 4286–4296, 2007.

[16] R. Ranjan, J. Y. Murthy, and S. V. Garimella, "Analysis of the wicking and thin-film evaporation characteristics of microstructures," *Journal of Heat Transfer*, vol. 131, no. 10, pp. 1–11, 2009.

[17] A. Bhattacharya, V. V. Calmidi, and R. L. Mahajan, "Thermophysical properties of high porosity metal foams," *International Journal of Heat and Mass Transfer*, vol. 45, no. 5, pp. 1017–1031, 2002.

[18] J. Thayer, "Analysis of a heat pipe assisted heat sink," in *Proceedings of the 9th International FLOTHERM Users Conference*, Orlando, Fla, USA, October 2000.

[19] B. Xiao and A. Faghri, "A three-dimensional thermal-fluid analysis of flat heat pipes," *International Journal of Heat and Mass Transfer*, vol. 51, no. 11-12, pp. 3113–3126, 2008.

[20] R. Boukhanouf, A. Haddad, M. T. North, and C. Buffone, "Experimental investigation of a flat plate heat pipe performance using IR thermal imaging camera," *Applied Thermal Engineering*, vol. 26, no. 17-18, pp. 2148–2156, 2006.

[21] Y. S. Muzychka, M. R. Sridhar, M. M. Yovanovich, and V. W. Antonetti, "Thermal spreading resistance in multilayered contacts: applications in thermal contact resistance," *Journal of Thermophysics and Heat Transfer*, vol. 13, no. 4, pp. 489–494, 1999.

[22] S. J. Kline and F. A. McClintock, "Describing uncertainties in single sample experiments," *Mechanical Engineering*, vol. 75, pp. 3–8, 1953.

Hindawi Publishing Corporation
Advances in Mechanical Engineering
Volume 2013, Article ID 287963, 9 pages
http://dx.doi.org/10.1155/2013/287963

Research Article

Numerical Determination of Effects of Wall Temperatures on Nusselt Number and Convective Heat Transfer Coefficient in Real-Size Rooms

Ozgen Acikgoz and Olcay Kincay

Yildiz Technical University, Mechanical Engineering Department, Barbaros Bulvari, Besiktas, 34349 Istanbul, Turkey

Correspondence should be addressed to Ozgen Acikgoz; oacikgoz@yildiz.edu.tr

Received 28 December 2012; Accepted 20 March 2013

Academic Editor: Ahmet Selim Dalkılıç

A modeled room was numerically heated from a wall and cooled from the opposite wall in order to create a real-room simulation. The cooled wall simulated heat loss of the room, and the heated wall simulated the heat source of enclosure. The effects of heated and cooled wall temperatures on convective heat transfer coefficient (CHTC) and Nusselt number in the enclosure were investigated numerically for two- (2D) and three-dimensional (3D) modeling states. Different hot wall and cold wall temperatures were applied in order to obtain correlations that contained characteristic length in Rayleigh numbers. Results were compared with the results of previously reported correlations that have been suggested for vertical room surfaces in enclosures. In addition, new correlations for Nusselt number and average CHTC for enclosures for isothermal boundary conditions within indicated Rayleigh number ranges were derived through solutions. Average deviations of new correlations obtained for CHTC and Nusselt number from the numerical data were found 0.73% and 1.76% for 2D study, 3.01% and 0.49% for 3D study. It was observed that the difference between the 2D and 3D solutions in terms of CHTC and Nusselt number was approximately 10%.

1. Introduction

Because of their importance in industry and living places, natural convection and temperature and velocity distribution problems in enclosures have been widely studied not only numerically but also experimentally in appropriate real-size building geometries. In the era in which we have been encountering many energy crises, natural convection problems in real-size rooms also has great importance since it remarkably affects energy consumption in buildings. Heating and cooling systems with vertical walls, floor, and ceiling (radiant panels) have not been extensively utilized for many years. Nevertheless, especially heating technologies with low water temperature have begun to be reassessed due to the austere energy policies pursued by governments throughout the world. As well as the progression of renewable energy techniques and low temperature heating systems, improving computational methods and descending solution periods for calculation of natural convection problems in real-size building rooms provide us to use computational fluid dynamics (CFD) programs in order to obtain convective heat transfer coefficients (CHTCs) using proper numerical solution preferences. Although conduction and radiation heat transfer simulation models in room size enclosures have been thoroughly described by numerous researchers, in convection there are still some uncertainties. Difficulties in accurate convection modeling especially analytical and numerical methods arise from complexity of the enclosure geometry, solution of fluid dynamics problems (governing equations), and differences at each air flow pattern in each heating choice.

ASHRAE HVAC Systems and Equipment Handbook—Fundamentals Handbook [1] lists many CHTC values and correlations. However, these equations were derived with the assumption that CHTC in an enclosure is equal to free edge isolated plates. Nonetheless, air flows at surrounding walls, even if they are not heated or cooled, affect the flows on adjacent walls. Also, the air flow on all surfaces affects the overall flow pattern in the enclosure. Thus, correlations for free plates cannot be accurately used for natural convection

problems in enclosures [2]. It can also be correlations derived through 2D enclosure modeling that cannot be utilized due to adjacent wall effects that are neglected in analytical expressions or numerical procedures.

Furthermore, experimental and computational studies have revealed that convection CHTCs of real-room surfaces are affected by the depth or height of the room, boundary conditions of the surface, smoothness/roughness of surfaces, and whether forced convection is present in the room.

In their study, Beausoleil-Morrison [3] showed the effect of CHTC correlations over building heating load predictions. They conducted experimental studies in a well-insulated test buildings that had radiant heating systems. Utilizing measurements from these test buildings and many different CHTC correlations, Beausoleil-Morrison found an 8% difference among the different simulations. He also found that building load amounts were more sensitive to CHTC correlations and the control set point of the room than to building fabric thermal properties or air infiltration. Peeters et al. [2] published an extensive review on experimentally derived CHTCs in enclosures and over free plates. They classified these correlations according to heating conditions, flow intensity, and also reference temperature preference in the enclosure. They questioned robustness of the correlations derived by numerous researchers and carried out new experiments in order to validate correlations. They concluded that large discrepancies were present among existing correlations in the literature. The differences were attributed to values of predicted coefficients, chosen reference air temperatures, and formats of the correlations. They also indicated that determination of appropriate choice of characteristic length was crucial. Nonetheless, it was asserted that choice of these parameters in building simulation programs was limited due to the common single node approach.

Awbi and Hatton [4] studied natural convection in two different enclosures. The enclosures' dimensions were 2.78 by 2.30 by 2.78 m and 1.05 by 1.01 by 1.05 m. One wall in each of the enclosure was used as a "heat sink" through an air conditioner placed in a small room next to the large enclosure. Opposite and adjacent walls to the "heat sink" wall have been heated with impregnated flexible sheets that had a 200 W/m^2 output. Thermal sensors were located inside on both sides of the surfaces. The aim of placing sensors on the outer surface of the enclosure was to calculate heat loss from heated surfaces. Reference air temperature for wall heating system was determined as 100 mm from heated surface and defined as "undisturbed air temperature" or in other words the temperature outside the thermal boundary layer. Thermal radiation was calculated through measuring emissivity of the surfaces and was extracted from total heat flux. Because they also heated the walls partially, characteristic length was determined as equal to hydraulic diameter. The results demonstrated that CHTCs of the heated wall were lower for the small enclosure that had a volume of approximately 1 m^3 than for the larger enclosure. Nonetheless, in order to assess whether the difference was because of the heating plate sizes or enclosure sizes, more experiments were carried out with small plates placed on surfaces. From these experiments, it was determined that there was a close agreement between CHTCs calculated with whole wall heated and CHTCs calculated with small plates heated. Consequently, the authors asserted that rather than the heated area on a wall, the size of the enclosure significantly affects CHTC. They also compared their results with the correlations in the extant literature and found that their data fell in the middle of the curves. The correlations that they suggested for walls are presented in Table 1.

Awbi [8] presented the results of a CFD study on natural CHTCs of a heated wall, a heated floor, and a heated ceiling. Two turbulence models were used: standard k-ε model using wall functions and low Reynolds k-ε model. The results were compared with experimental results.

Fohanno and Polidori [9] aimed to develop a theoretical model of convective heat transfer between an isolated vertical plate and natural convective flow. They assumed a constant heat flux on surface, and the model they produce allowed average and local CHTCs to be calculated in laminar and turbulent regime. The correlation they derived for average CHTC was produced through local CHTC results. They indicated that there was a good agreement between Alamdari and Hammond's correlations. The applicability of the new correlations to real-size buildings was considered, and despite the three-dimensionality of real-size rooms, a 10% difference was found between data taken from experimental and mathematical work.

To calculate CHTCs for all surfaces in an enclosure, Khalifa and Marshall [5] utilized an experimental enclosure that had dimensions similar to those of a real-size room. Sixty-five aluminium thermistors were used to measure air and surface temperatures in the enclosure. Inner and outer surfaces of the enclosure were coated with aluminium. Radiant heat exchange was not counted in the CHTC calculation process. Also, a sensitive uncertainty analysis was employed. In this analysis, temperature measurements, conductivity of the materials, and the lack of inclusion of long wave radiation in the low emissivity chamber were considered in order to take account of all possible error sources [2]. They derived many general correlations, including the two that are presented in Table 1.

Khalifa and Khudheyer [10] conducted an experimental investigation on the effects of 14 different configurations of partitions on natural convection heat transfer in enclosures. Like other studies, the experiment considered vertical hot and cold walls, while the other walls were insulated. Investigation was conducted for Rayleigh numbers between $6 \cdot 10^7$ and $1.5 \cdot 10^8$ with the aspect ratio of 0.5. Correlations for the test configurations were derived. Khalifa [11] presented an extensive review of studies regarding isolated vertical and horizontal surfaces. Comparisons between correlations for heat transfer coefficients were conducted, and the discrepancies were determined to be up to a factor of 2 for isolated vertical surfaces, up to a factor of 4 for isolated horizontal surfaces facing upward, and up to a factor of 4 for isolated horizontal surfaces facing downward.

Khalifa [12] presented a wide review of two- and three-dimensional natural convection problems, focusing primarily

Table 1: Correlations derived for CHTC and Nusselt number in enclosures.

Correlation	Conditions	Reference temperature
Awbi and Hatton [4] $h = \frac{1.823}{D^{0,121}}(\Delta T)^{0,293}$ $\mathrm{Nu} = 0.289(\mathrm{Gr})^{0,293}$	Heated wall (2.78 × 2.30 × 2.78 m)	Local air temperature (100 mm from wall)
Khalifa and Marshall [5] $h = 2.3(\Delta T)^{0,24}$	For a room with a heated wall and a room heated by a radiator under a window (2.35 × 2.95 × 2.08 m)	Average room temperature
$h = 2.10(\Delta T)^{0,23}$	For a room heated by a fan heater (2.35 × 2.95 × 2.08 m)	Average room temperature
ASHRAE [1] $\mathrm{Nu} = 0.117(\mathrm{Gr})^{0,117}$	Turbulent flow $10^8 < \mathrm{Gr} < 10^{12}$ (for free plate)	Average room temperature
Li et al. [6] $h = 3.08(\Delta T)^{0,25}$	Normal conditions, occupied room	Average room temperature
Min et al. [7] $h = 1.646\frac{(\Delta T)^{0,32}}{H^{0,05}}$	Heated floor or heated ceiling	Average room temperature

Table 2: Change of Nusselt numbers and CHTCs at various wall temperatures (2D solution results, $L \times H \times L = 4.00 * 2.85 * 4.00$ m).

T_H (°C)	$T_c = 5$°C			$T_c = 10$°C			$T_c = 15$°C		
	Ra	Nu	h (W/m^{2}K)	Ra	Nu	h (W/m^{2}K)	Ra	Nu	h (W/m^{2}K)
20	$1.1E+11$	721.52	4.53	$7.03E+10$	614.2	3.88	$3.38E+10$	472.16	3.01
25	$1.41E+11$	783.07	4.96	$1.01E+11$	695.23	4.43	$6.51E+10$	590.85	3.8
30	$1.69E+11$	832.38	5.31	$1.3E+11$	754.31	4.85	$9.39E+10$	669.71	4.34
35	$1.95E+11$	870.14	5.59	$1.57E+11$	801.39	5.2	$1.21E+11$	727.26	4.75

on heat transfer in buildings. He determined the discrepancies between correlations to be up to a factor of 5 for vertical surfaces, a factor of 4 for horizontal surfaces facing upward, and up to a factor of 8 for horizontal surfaces facing downward.

In their study, which can be considered as the first experimental investigation for CHTCs in enclosures, Min et al. [7] studied within the range of Rayleigh number 10^9 to 10^{11} and with enclosure dimensions 3.60 by 7.35 by 2.40 m, 3.60 by 7.35 by 3.60 m, and 3.60 by 3.60 by 2.40 m. These correlations were derived for nonventilated conditions. Surfaces which were not heated were kept at constant temperature. Temperatures of the surfaces and heat fluxes applied to the enclosure were measured. Also, radiation effects were recorded. While the temperatures of the surfaces that were not heated varied between 4.4°C and 21.1°C, temperatures of floor surfaces varied between 24°C and 43.3°C and temperatures of ceiling surfaces varied between 32.2°C–65.6°C [2].

Li et al. [6] investigated natural convection in an occupied office room with normal working conditions up to a temperature difference of 1.5°C.

Karadağ [13] numerically investigated the relationship between radiation and convection heat transfer coefficients at ceilings when the floor surface was isolated. To achieve this goal, first Karadağ neglected radiative heat transfer at surfaces ($\varepsilon_w = \varepsilon_c = 0$) for different room sizes (3 by 3 by 3 m, 4 by 3 by 4 m, and 6 by 3 by 4 m) and thermal boundary conditions (T_c = 0–25°C, T_w = 28–36°C). Then Karadağ determined radiative heat transfer for different surface emissivities ($\varepsilon_w = \varepsilon_c$ = 0.7-0.8 and 0.9). Numerical data were compared with results in the literature. The ratios of radiative heat transfer to convective heat transfer coefficients were calculated, and it was observed that ratios varied from 0.7 to 2.3.

Karadağ et al. [14] numerically analyzed changes in Nusselt number with ceiling and floor temperatures and room dimensions. While wall temperatures were kept at constant, ceiling temperature ranged from 10 to 25°C for different room dimensions. It was observed that when the temperature between the ceiling and air was raised, the Nusselt number over the floor also increased. Correlations in the literature that did not take into account the ceiling and floor temperatures deviated up to 35% from the results of this study. As a result, it was indicated that a new correlation for Nusselt number over the floor that encompasses the effect of thermal conditions and all room dimensions must be explored.

Although many other laminar regime natural problems in an enclosure have been solved in the literature, the turbulence natural convection problem in an enclosure of a similar size as a real room that was heated from one wall and cooled from the opposite wall has not been thoroughly researched with numerical methods, especially due to the length of solution periods. The main purpose of this study is to numerically investigate the effect of hot and cold wall temperatures of the room and characteristic length on average Nusselt number and CHTC for an enclosure modeled two- and three-dimensionally. Then, the results were compared with the correlations in the literature that are presented in Table 1.

Table 3: Change of Nusselt numbers and CHTCs at various wall temperatures (3D solution results, $L \times H \times L = 4.00 * 2.85 * 4.00$ m).

T_H (°C)	$T_c = 5$°C			$T_c = 10$°C			$T_c = 15$°C		
	Ra	Nu	h (W/m^{2}K)	Ra	Nu	h (W/m^{2}K)	Ra	Nu	h (W/m^{2}K)
20	$1.1E+11$	647.11	4.06	$7.03E+10$	550.66	3.48	$3.38E+10$	423.68	2.7
25	$1.41E+11$	703.08	4.44	$1.01E+11$	623.9	3.98	$6.51E+10$	530.78	3.41
30	$1.69E+11$	747	4.76	$1.3E+11$	677.82	4.35	$9.39E+10$	601.35	3.89
35	$1.95E+11$	781.9	5.02	$1.57E+11$	720.13	4.66	$1.21E+11$	653.27	4.26

The enclosure's right and left walls were heated and cooled with constant wall temperature, while the other walls of the enclosure were kept adiabatic with the heat flux input "0 W/m^2".

2. Numerical Method and Mathematical Formulation

Because of long solution periods of governing equations in large geometries, utilization of computational fluid dynamics (CFD) programs has not been practical until a few years ago. However, today's improving computer technology allows us to utilize CFD programs in this field. Despite the frequent mesh density in the boundary layers of room model, CFD programs provide results in reasonable periods, especially in 2D solutions but also in 3D solutions. In this study, we examined numerical methods for calculating average Nusselt number and CHTCs over the heated wall of an enclosure that had similar dimensions to a room of a building. 2D and 3D natural convection problems in enclosure with the dimensions of 4.00 by 2.85 by 4.00 were considered. In order to acquire similar wall temperatures with wall heating systems, the heated sidewall was heated within the range of 20°C to 35°C, while cooled sidewall was cooled to the temperatures between 5°C–15°C. The other walls of the enclosure were kept adiabatic.

The most significant aspect of solving a heat transfer problem in a real-size room by means of a CFD program is to model and properly mesh of the enclosure. For 2D and 3D modeling the enclosure, GAMBIT 2.4.6, a modeling and meshing program, was chosen. In simple geometries as in this study's model, quad/hex meshes provide more qualified solutions with fewer cells than a tri/tet mesh. Thus, all the surfaces of the enclosure were chosen as plane quad/hex meshes in this study. To decrease the meshing effects on the results in each modeling type (two- and three- dimensional) edges of both 2D and 3D modeled rooms have been meshed with different "interval counts." In order to observe whether the mesh effect has been widely diminished, Nusselt numbers were taken from FLUENT for each modeling condition. Since, the difference between the last two solutions is so small, the interval count before the last one (120×100) was chosen as appropriate number. In the 2D model, distance between heated and cooled walls (characteristic length, $L = 4{,}0$ m) was divided into 120 intervals. These intervals were preferred to be frequent near walls due to the rapid temperature differences in surface boundary layers; nonetheless, the intervals were determined less frequent towards the center of the model (Figures 1 and 2) due to the fact that temperature fluctuation from outside of the boundary layer to center of the room is approximately zero, as can be seen in Figure 3. To achieve this, "first length"—the ratio of midpoint interval size at the edge to the first interval size at the corner of edge—was determined as 0.001. Also, in 3D solution, various interval counts on three axes were employed and appropriate interval counts were found ($45 \times 40 \times 20$). Air was chosen as the fluid existing in the enclosure.

FLUENT 6.3 software, one of the most common used codes, was utilized to solve governing equations (energy, momentum, continuity, and turbulence). The program's solution technique is focused on control volume theory turning governing equations into algebraic equations in order to solve them. The control volume technique works by integrating the governing equations for each control volume and then generating discretization of the equations, which conserve each quantity based on control volume [15]. In the model, the key dimension used is characteristic length ($L = 4.0$ m)—which is the difference between heated and cooled walls, that is opposite walls. According to characteristic length, the Rayleigh numbers for the system were calculated, as shown in (1) for one example.

Full Rayleigh numbers table can be seen in Tables 2 and 3. Because all the Rayleigh numbers calculated were greater than 10^9, a turbulence model was applied in the flow pattern. The first order upwind scheme was utilized to discretize governing equations. The under relaxation factors for density, momentum, turbulence kinetic energy, turbulence dissipation rate, turbulent viscosity, and energy (1.0, 2.0, 0.8, 0.8, 1, and 0.9) were preferred to converge the solution. Simulations were performed on a laptop with an Intel Core i5 processor and the following specifications −2430 M CPU 2.40 GHz, 6 GB Ram, Windows 7 Home Basic 64 Bit SP1 operating system. The required solution period for each appropriate (meshing effect minimized) grid model was about 12 hours:

$$\mathrm{Ra} = \frac{g\beta L^3 \left(T_H - T_C\right)}{\nu\alpha} = \frac{9.81 \times 0.0034 \times 4^3 \left(30 - 10\right)}{15.26 \times 10^{-5} \times 2.15 \times 10^{-5}} = 1.3 \times 10^{11} > 10^9. \quad (1)$$

The governing equations for turbulence 3D flow can be written as follows.

Continuity equation:

$$\frac{\partial u}{\partial x} + \frac{\partial v}{\partial y} + \frac{\partial w}{\partial z} = 0. \quad (2)$$

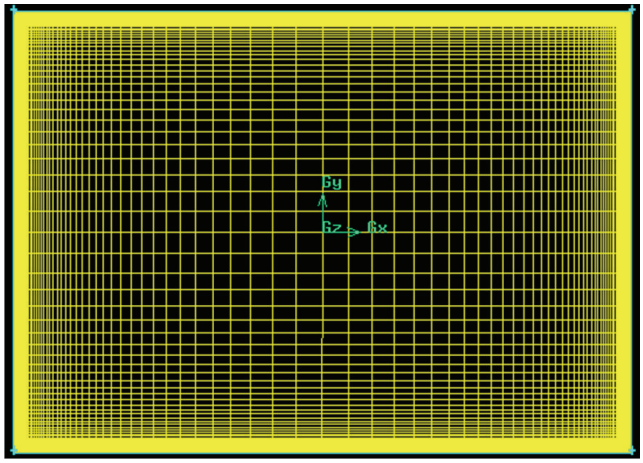

Figure 1: Meshing detail of two-dimensional room ($L \times H$ = 4,0 m × 2,85 m).

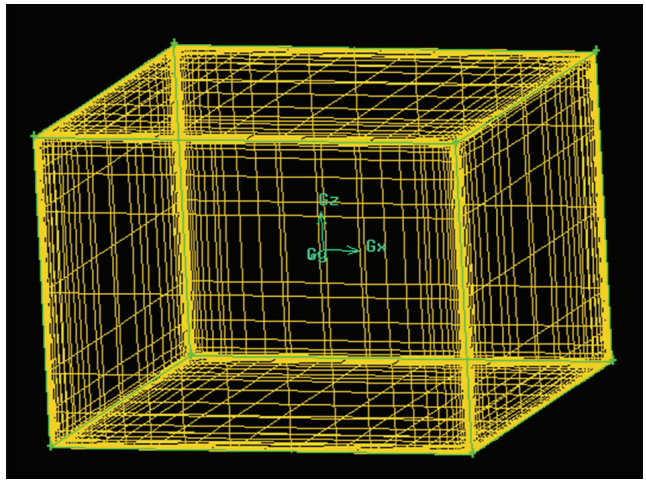

Figure 2: Meshing detail of three-dimensional room ($L \times H \times L$ = 4,0 m × 2,85 m × 4,0 m).

Momentum equations:

$$\rho\left(u\frac{\partial u}{\partial x}+v\frac{\partial u}{\partial y}+w\frac{\partial u}{\partial z}\right)=-\frac{\partial p}{\partial x}+\mu\left(\frac{\partial^2 u}{\partial x^2}+\frac{\partial^2 u}{\partial y^2}+\frac{\partial^2 u}{\partial z^2}\right)$$

$$\rho\left(u\frac{\partial v}{\partial x}+v\frac{\partial v}{\partial y}+w\frac{\partial v}{\partial z}\right)=-\frac{\partial p}{\partial y}+\mu\left(\frac{\partial^2 v}{\partial x^2}+\frac{\partial^2 v}{\partial y^2}+\frac{\partial^2 v}{\partial z^2}\right)$$

$$\rho\left(u\frac{\partial w}{\partial x}+v\frac{\partial w}{\partial y}+w\frac{\partial w}{\partial z}\right)=-\frac{\partial p}{\partial z}+\rho g+\mu\left(\frac{\partial^2 w}{\partial x^2}+\frac{\partial^2 w}{\partial y^2}+\frac{\partial^2 w}{\partial z^2}\right). \quad (3)$$

Energy equation:

$$\rho\left(u\frac{\partial T}{\partial x}+v\frac{\partial T}{\partial y}+w\frac{\partial T}{\partial z}\right)=\alpha\left(\frac{\partial^2 T}{\partial x^2}+\frac{\partial^2 T}{\partial y^2}+\frac{\partial^2 T}{\partial z^2}\right). \quad (4)$$

Residual values were determined as 10^{-6} for energy and 10^{-3} for momentum and continuity equations. The physical properties of air (thermal conductivity, specific heat, density, and viscosity) in the room were written into the program as the average temperature value of hot and cold walls from Incropera and DeWitt's physical properties of air tables [15].

FLUENT has two different solver types, "Pressure Based" and "Density Based." In this study, we chose "Density Based," and the Boussinesq approach was applied. Among many viscous models presented by the program, as suggested by Karadağ [13], "k-ε" was chosen, and the model of "k-ε" was indicated as "standard" which was utilized by Awbi as well. Studies in the literature suggest that the k-ε standard model is the most appropriate for natural convection. It is the most widely used engineering turbulence model for industrial applications, as it is robust and reasonably accurate and contains submodels for compressibility, buoyancy and combustion, and so forth. Also, it is suitable for initial iterations, initial screening of alternative designs, and parametric

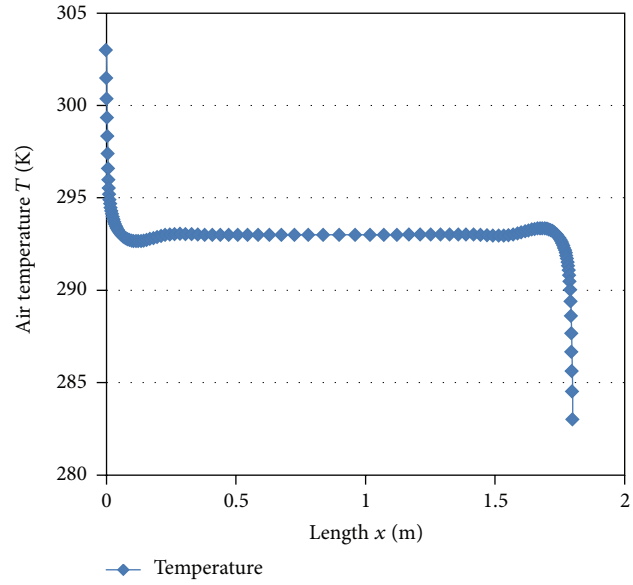

Figure 3: Temperature variation along the center of enclosure, from midpoint of hot wall to cold wall ($L \times H \times L$ = 4,0 × 2.85 × 4,0 m).

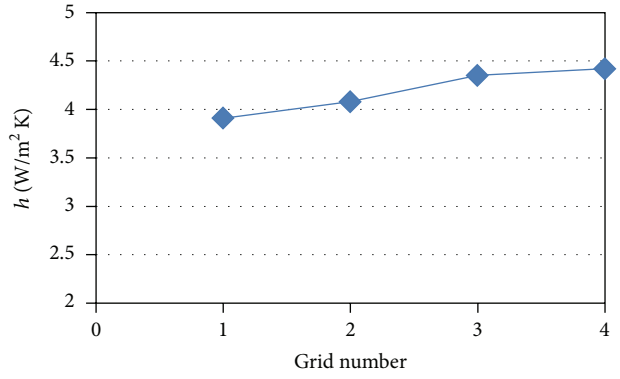

Figure 4: Grid independency of 2D results in terms of CHTC.

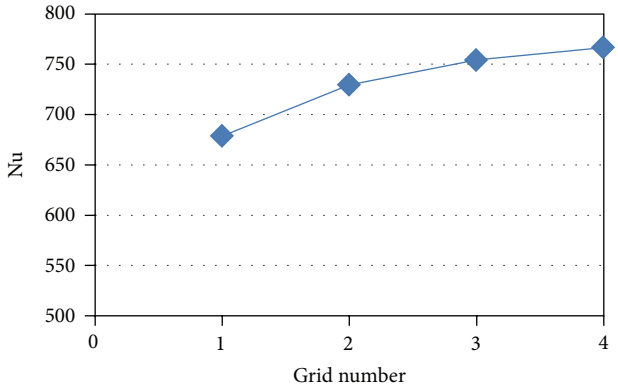

Figure 5: Grid independency of 2D results in terms of Nu.

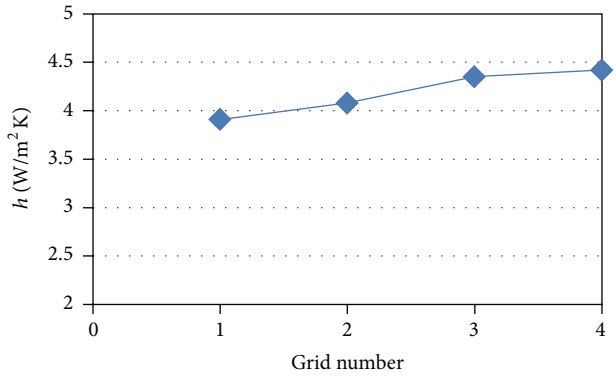

Figure 6: Grid independency of 2D results in terms of CHTC.

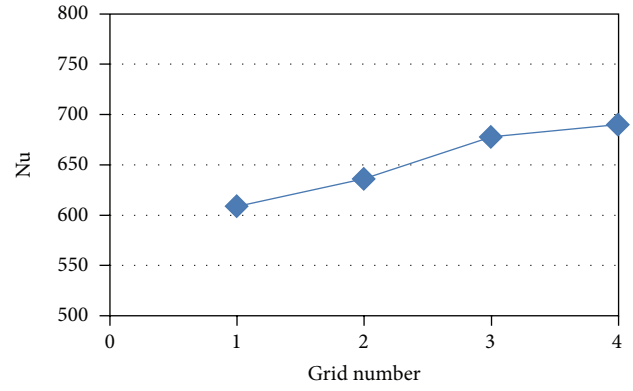

Figure 7: Grid independency of 2D results in terms of Nu.

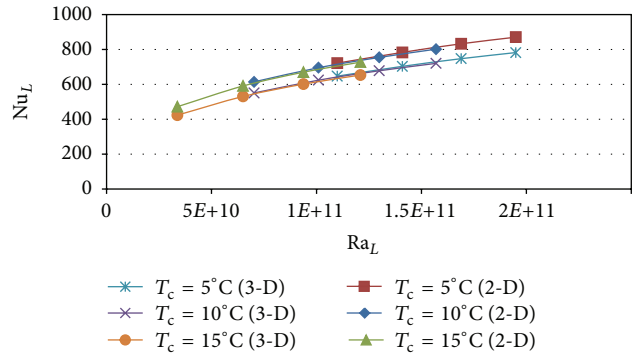

Figure 8: Change of Nusselt number at different cold wall temperatures (T_c = 5–15°C, T_H = 20–35°C, $L \times H \times L$ = 4.0 × 2.85 × 4.0 m).

studies, like this study: Fluent User's Guide, Introductory FLUENT v6.3 notes [16]. Turbulence kinetic energy, k, and dissipation rate, ε, have been calculated through the transport equations (5) and (6), respectively,

$$\frac{\partial}{\partial x}(\rho k u) = \frac{\partial}{\partial y}\left(\left[\left(\mu + \frac{\mu_t}{\sigma_k}\right)\frac{\partial k}{\partial y}\right]\right) + G_k - \rho\varepsilon \quad (5)$$

$$\frac{\partial}{\partial x}(\rho \varepsilon u) = \frac{\partial}{\partial y}\left(\left[\left(\mu + \frac{\mu_t}{\sigma_\varepsilon}\right) + \frac{\partial \varepsilon}{\partial y}\right]\right) + C_{\varepsilon 1}\frac{\varepsilon}{k}G_k - \rho C_{\varepsilon 2}\frac{\varepsilon^2}{k}, \quad (6)$$

where

$$\mu_t = \rho c_p \frac{k^2}{\varepsilon}$$
$$G_k = -\rho\overline{v'u}\frac{\partial v}{\partial x}, \quad (7)$$

where $C_{1\varepsilon}$ and $C_{2\varepsilon}$ are constants. σ_k and σ_ε are the turbulent Pr numbers for k and ε, respectively. Also, k-ε model constants, C_μ, $C_{\varepsilon 1}$, $C_{\varepsilon 2}$, σ_k, and σ_ε are equal to 0.09, 1.44, 1.92, 1.0, and 1.3, respectively (Fluent User's Guide, Introductory FLUENT v6.3 notes [16], Yılmaz and Öztop [17]).

Because the object of study was to find average CHTC and because the program gives CHTC with surface radiation heat transfer coefficient and these two could not be separated from each other, no radiation model was chosen from the "models" section of the program. In FLUENT, thermal boundary conditions can be defined with five different methods: constant heat flux, constant temperature, convection, radiation, and mixed. In this study, the wall surfaces that were not heated and cooled were assumed adiabatic and defined as "0 W/m^2" to reach adiabatic boundary conditions in the program. In addition, thermal boundary conditions of heated and cooled walls that stood opposite were defined at a constant temperature. As suggested by Karadağ et al. [14], the surface Nusselt numbers of the heated walls were examined as references to decide whether the meshing effect on results was diminished. In Figures 4–7 the CHTC and Nu number results that were obtained at different interval counts were presented and as stated above the optimum interval counts for 2D and 3D models were determined (120 × 100) and (45 × 40 × 20), in other words, "Grid Number 3," because the difference between the last two grid number preferences is approximately 1%. To reduce the solution period and since the difference is about 1%, "Grid Number 4" was not chosen as the appropriate model.

Average Nusselt number and CHTC in the enclosure are calculated through the program's "area weighted average" speciality function and β, α, and γ are calculated at film temperature, namely, the average temperature of hot and cold wall temperatures. If we calculate the Rayleigh number for the

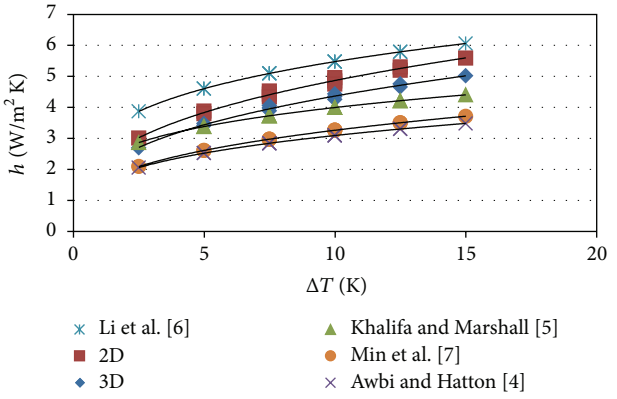

FIGURE 9: Change of CHTC at various temperature difference values between hot and cold walls (T_c = 5–15°C, T_H = 20–35°C, $L \times H \times L$ = 4.0 × 2.85 × 4.0 m).

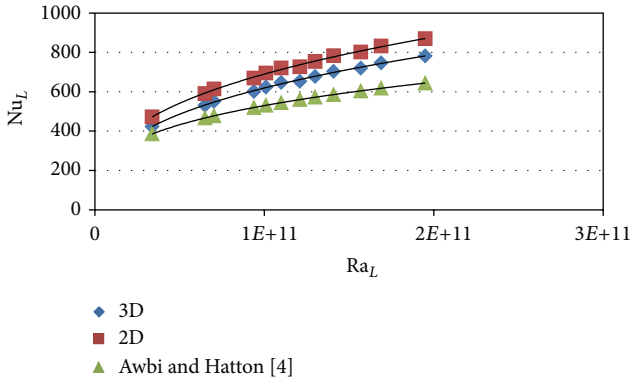

FIGURE 10: Variation of Nusselt number with Rayleigh number in the enclosure ($L \times H \times L$ = 4,0 × 2,85 × 4,0 m).

4,0 by 2,85 by 4,0 m room that can be seen in Figures 1 and 2 when hot and cold wall temperatures are 30°C and 10°C, respectively, it can be seen that Rayleigh number is above 10^9, and consequently the flow pattern present in the room is turbulent. All calculated Rayleigh numbers at various wall temperatures are presented in Tables 2 and 3. Also, Nusselt numbers and CHTCs at corresponding Rayleigh numbers have been presented in these tables.

3. Results and Discussion

Computational solutions were conducted according to the depictions which were mentioned previously in Section 2. In these solutions, different hot and cold wall temperatures were applied in order to acquire various points on the Nusselt-Rayleigh number diagrams. Figure 8 illustrates the change of hot wall surface average Nusselt number with variation of cold wall temperatures for one constant room dimension (4.0 by 2.85 by 4.0 m), for both (2D) and (3D). The approximate difference between these results is 10% as also can be seen from Tables 2 and 3. It is obvious from the figures that when the cold wall temperature increases, the temperature difference between the hot wall and cold wall decreases, and thus the Nusselt number over the hot wall also decreases. Therefore, it can be stated that the temperature of cold wall in a room affects the Nusselt number and CHTC in the enclosure.

In Figures 8–10, results of this numerical study, implemented through FLUENT, for appropriate hot and cold wall temperatures similar to real wall temperatures in buildings (hot and cold wall temperatures for real-room surfaces) were compared with the results of correlations presented in the literature. For all the Rayleigh numbers that were presented in Tables 2 and 3, corresponding Nusselt numbers were obtained through the program and are illustrated in Figure 10. It can be deduced that in addition to the Rayleigh number, the Nusselt number depends on hot and cold wall temperatures. According to all these obtained numbers and Figure 10 we have derived two new Nusselt number correlations (8) for an enclosure similar with a real-size room of a building within a Rayleigh number range between $3.38 \cdot 10^9$ and $1.95 \cdot 10^{11}$, while the temperature difference variant of Rayleigh number has been defined as the difference between hot and cold wall temperatures:

$$\begin{aligned} \mathrm{Nu}_L &= 0.1\mathrm{Ra}_L^{0,349} \quad \text{(2D solution)} \\ \mathrm{Nu}_L &= 0.09\mathrm{Ra}_L^{0,349} \quad \text{(3D solution)}. \end{aligned} \tag{8}$$

As the deviations of these new correlations from the Nusselt numbers obtained via 2D and 3D numerical study are 1.76% and 0.49%, deviations of 2D and 3D results from Awbi and Hatton's [4] correlation are 19.34% and 13.43%, respectively. Although 2D solutions have a much more sophisticated meshing infrastructure, 3D solution has a closer agreement with Awbi and Hatton's [4] experimental work. This situation can be explained with "adjacent wall effects." Similar with vertical plate correlations presented and utilized for many years in the literature, 2D solutions also have a disadvantage. In 2D solutions, although the effect of x and y axis can be assessed, third side effect, in other words, "depth of the enclosure," cannot be counted in the solution progression. Studies published in the literature show that all surrounding walls in the enclosure affect CHTCs, since they have significant effect on flow pattern. Hence, the difference between Awbi and Hatton's [4] experimental work and the 3D solutions of this study has better agreement than the 2D solution results as can be seen in Figure 9, although two-dimensional has more detailed meshing frequency especially near walls. Differences may also be interpreted with measurement precision quality of compared experimental study.

Two novel correlations were derived and presented in the figure, written as (9). It can be discerned that CHTC in an enclosure varies with temperature difference between room centre and heated or cooled wall. Figure 9 shows that discrepancies of 3D results of this study and the results of Khalifa and Marshall [5], Li et al. [6], Min et al. [7], and Awbi and Hatton [4] are 6.38%, 21.66%, 25.05%, and 27.7%, respectively. Differences between this study and the aforementioned studies can be interpreted as follows. In Min et al. [7] study no heating equipment on the vertical walls was utilized. Rather, the study used "heated floor on heated ceiling" and the difference can be explained due to this preference. Li et al. [6] worked in an "occupied room under

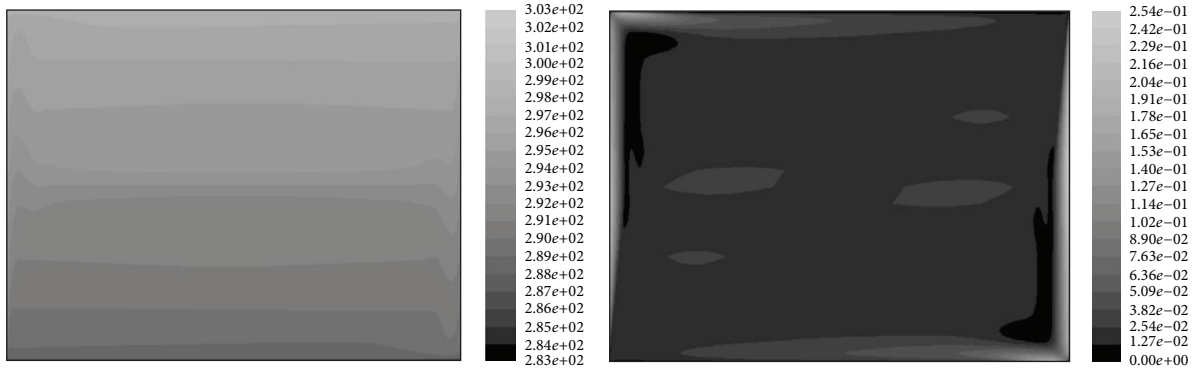

(a) (b)

Figure 11: CFD predictions of temperature (K) and velocity magnitude (m/s) contours of 2D model's results, respectively (T_H = 30°C, T_C = 10°C; $L \times H \times L$ = 4.0 × 2.85 × 4.0 m).

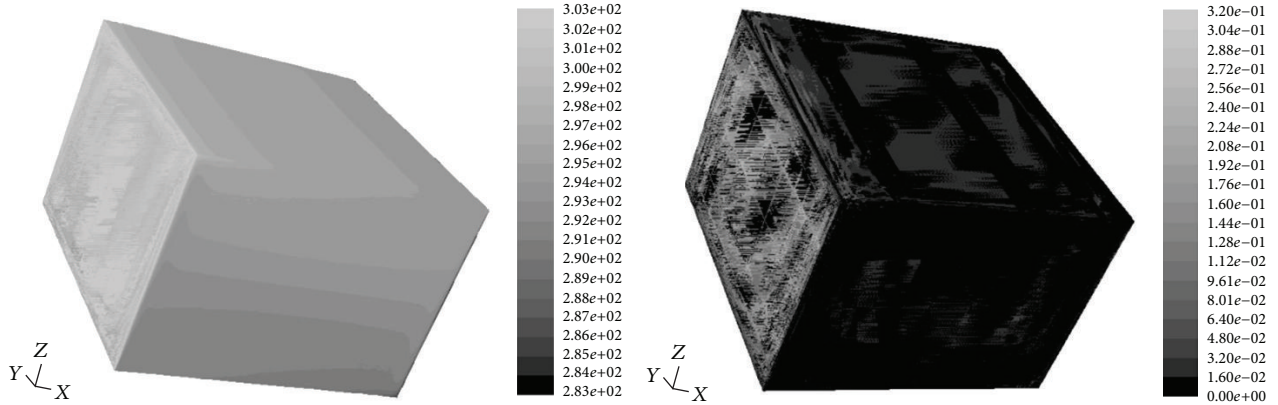

(a) (b)

Figure 12: CFD predictions of temperature (K) and velocity magnitude (m/s) contours of 3D model's results, respectively (T_H = 30°C, T_C = 10°C; $L \times H \times L$ = 4.0 × 2.85 × 4.0 m).

normal conditions," which could have caused the differences. Although Awbi and Hatton's [4] comprehensive study is the most similar to the present work, the researchers of the study preferred "constant heat flux" (200 W/m^2) on vertical walls as boundary conditions. It is thought that this choice could bring about the discrepancy between the two studies. Results have not been compared with correlations derived for free plates, because, as previously stated, it was not appropriate to compare free plate results with enclosure results due to adjacent wall effects:

$$\begin{aligned} h &= 2.21\Delta T^{0,343} \quad \text{(2D solution)} \\ h &= 1.98\Delta T^{0,343} \quad \text{(3D solution)}. \end{aligned} \tag{9}$$

In addition, in Figures 11 and 12, 2D and 3D temperature and velocity flow patterns for the studied enclosure can be seen, respectively. Also, according to 2D and 3D models, maximum velocity in the room was found 0.27 m/s and 0.32 m/s, respectively. Both values are about 0.25 m/s, that is, the comfort velocity value in the rooms. Furthermore, velocity at overwhelming part of the enclosure is approximately zero.

4. Conclusions

Numerical case studies have been implemented to acquire Nusselt number and CHTC points on Rayleigh-Nusselt and CHTC-ΔT diagrams within the Rayleigh number range of $3.38 \cdot 10^9$ to $1.95 \cdot 10^{11}$. To attain different points on diagrams and to observe the convective heat transfer behavior in the enclosure, different heated and cooled wall temperatures were applied. Since, all the Rayleigh numbers are above 10^9, the study involves the area of turbulent convective heat transfer. This study has shown that many correlations are produced by room surfaces, particularly for heated and cooled vertical wall surfaces. Also, two new correlations were derived for both average CHTC and Nusselt number in an enclosure which has the dimensions of 4.00 by 2.85 by 4.00 and heated from one vertical wall and cooled from the opposite wall in order to consist a real-room situation.

The results obtained with this study lie within the range of data obtained from other correlations. The differences between correlation results are thought to be caused by reference temperature determination, whether the study considers

3D or 2D and heat losses and gains that could not be counted by some experimental studies.

Energy consumption and thermal comfort in buildings have great impact on people's productivity, and these factors must be combined at some point. Therefore, parameters for calculating heating and cooling loads in buildings must be well investigated. Correct usage of CHTC does significantly affect losses from wall surfaces to the atmosphere. Also, CHTCs are used with the conduction loss of windows while calculating their total heat transfer coefficient. The effect of correct usage has a significant impact on total heat loss amounts. Also, correct usage has a great impact on thermal comfort in living spaces.

The study carries weight with the determination of the heating load in buildings as well. In this respect, it is thought that this study's results will also be useful for the thermal comfort and energy efficiency in buildings that use wall heating radiant systems and provide an appropriate direction to engineers who calculate heating load via package programs.

Nomenclature

$C_\mu, C_{\varepsilon 1}, C_{\varepsilon 2}, \sigma_k, \sigma_\varepsilon$: Model constants
C_p: Specific heat (J/kgK)
D: Diameter (m)
G: Generation of turbulence energy
H: Height (m)
h: Convective heat transfer coefficient, (W/m^2 K)
L: Length (m)
Nu: Nusselt number
p: Pressure (atm)
Ra: Rayleigh number
T: Temperature (K)
x, y, z: Coordinates
u, v, w: Velocities (m/s).

Greek Letters

ρ: Density, (kg/m^3)
ε: Emissivity, turbulence dissipation rate
Δ: Difference
μ: Dynamic viscosity (Ns/m^2)
μ_t: Turbulent viscosity (Ns/m^2).

Subscripts

C: Cold
H: Hot, hydraulic
k: Turbulent energy.

Acknowledgment

The authors gratefully acknowledge the financial support from the Scientific Research Projects Administration Unit of Yildiz Technical University (YTU-BAPK/27-06-01-03, 2007).

References

[1] "ASHRAE HVAC Systems and Equipment Handbook," in *Panel Heating and Cooling*, chapter 6, American Society of Heating Refrigeration and Air-conditioning Engineers, 2000.

[2] L. Peeters, I. Beausoleil-Morrison, and A. Novoselac, "Internal convective heat transfer modeling: critical review and discussion of experimentally derived correlations," *Energy and Buildings*, vol. 43, no. 9, pp. 2227–2239, 2011.

[3] Beausoleil-Morrison, "The adaptive simulation of convective heat transfer at internal building surfaces," *Building and Environment*, vol. 37, no. 8-9, pp. 791–806, 2002.

[4] H. B. Awbi and A. Hatton, "Natural convection from heated room surfaces," *Energy and Buildings*, vol. 30, no. 3, pp. 233–244, 1999.

[5] A. J. N. Khalifa and R. H. Marshall, "Validation of heat transfer coefficients on interior building surfaces using a real-sized indoor test cell," *International Journal of Heat and Mass Transfer*, vol. 33, no. 10, pp. 2219–2236, 1990.

[6] L. D. Li, W. A. Beckman, and J. W. Mitchell, "An experimental study of natural convection in an office room, large time results," Unpublished report, Solar Energy Laboratory, University of Wisconsin, Madison, Wis, USA, 1983.

[7] T. C. Min, L. F. Schutrum, G. V. Parmelee, and J. D. Vouris, "Natural convection and radiation in a panel heated room," *ASHRAE Transactions*, vol. 62, pp. 337–358, 1956.

[8] H. B. Awbi, "Calculation of convective heat transfer coefficients of room surfaces for natural convection," *Energy and Buildings*, vol. 28, no. 2, pp. 219–227, 1998.

[9] S. Fohanno and G. Polidori, "Modelling of natural convective heat transfer at an internal surface," *Energy and Buildings*, vol. 38, no. 5, pp. 548–553, 2006.

[10] A. J. N. Khalifa and A. F. Khudheyer, "Natural convection in partitioned enclosures: experimental study on 14 different configurations," *Energy Conversion and Management*, vol. 42, no. 6, pp. 653–661, 2001.

[11] A. J. N. Khalifa, "Natural convective heat transfer coefficient: a review I. Isolated vertical and horizontal surfaces," *Energy Conversion and Management*, vol. 42, no. 4, pp. 491–504, 2001.

[12] A. J. N. Khalifa, "Natural convective heat transfer coefficient: a review II. Surfaces in two- and three-dimensional enclosures," *Energy Conversion and Management*, vol. 42, no. 4, pp. 505–517, 2001.

[13] R. Karadağ, "The investigation of relation between radiative and convective heat transfer coefficients at the ceiling in a cooled ceiling room," *Energy Conversion and Management*, vol. 50, no. 1, pp. 1–5, 2009.

[14] R. Karadağ, I. Teke, and H. Bulut, "A numerical investigation on effects of ceiling and floor surface temperatures and room dimensions on the Nusselt number for a floor heating system," *International Communications in Heat and Mass Transfer*, vol. 34, no. 8, pp. 979–988, 2007.

[15] F. P. Incropera and D. P. DeWitt, *Fundamentals of Heat and Mass Transfer*, John Wiley & Sons, New York, NY, USA, 4th edition, 1996.

[16] "Introductory FLUENT v6.3 notes," 2006, http://www.fluentusers.com.

[17] I. Yılmaz and H. F. Öztop, "Turbulence forced convection heat transfer over double forward facing step flow," *International Communications in Heat and Mass Transfer*, vol. 33, no. 4, pp. 508–517, 2006.